

www.acsami.org Research Article

Probing Electrocatalytic Synergy in Graphene/MoS₂/Nickel Networks for Water Splitting through a Combined Experimental and Theoretical Lens

Dipankar Saha, Ayush Bhardwaj, Jiacheng Wang, Varun Pande, Robert Hengstebeck, Peng Bai,* and James J. Watkins*



Cite This: ACS Appl. Mater. Interfaces 2024, 16, 42254-42269



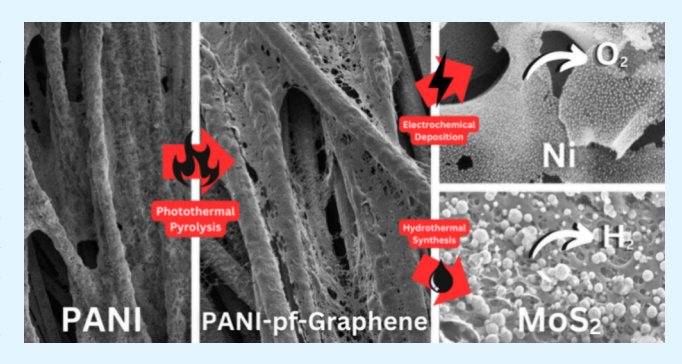
ACCESS

III Metrics & More

Article Recommendations

Supporting Information

ABSTRACT: The development of low-cost and active electrocatalysts signifies an important effort toward accelerating economical water electrolysis and overcoming the sluggish hydrogen or oxygen evolution reaction (HER or OER) kinetics. Herein, we report a scalable and rapid synthesis of inexpensive Ni and MoS₂ electrocatalysts on N-doped graphene/carbon cloth substrate to address these challenges. Mesoporous N-doped graphene is synthesized by using electrochemical polymerization of polyaniline (PANI), followed by a rapid one-step photothermal pyrolysis process. The N-doped graphene/carbon cloth substrate improves the interconnection between the electrocatalyst and substrate. Consequently, Ni species deposited on an N-doped



graphene OER electrocatalyst shows a low Tafel slope value of 35 mV/decade at an overpotential of 130 mV at 10 mA/cm² current density in 1 M KOH electrolytes. In addition, Ni-doped MoS₂ on N-doped graphene HER electrocatalyst shows Tafel slopes of 37 and 42 mV/decade and overpotentials of 159 and 175 mV, respectively, in acidic and alkaline electrolytes at 10 mA/cm² current density. Both these values are lower than recently reported nonplatinum-group-metal-based OER and HER electrocatalysts. These excellent electrochemical performances are due to the high electrochemical surface area, a porous structure that improves the charge transfer between electrode and electrolytes, and the synergistic effect between the substrate and electrocatalyst. Raman spectroscopy, X-ray photoelectron spectroscopy, and density functional theory (DFT) calculations demonstrate that the Ni hydroxide species and Ni-doped MoS₂ edge sites serve as active sites for OER and HER, respectively. Finally, we also evaluate the performance of the HER electrocatalyst in commercial alkaline electrolyzers.

KEYWORDS: electrocatalysts, oxygen evolution reaction, hydrogen evolution reaction, nickel, 2D materials, MoS₂, theoretical calculations

INTRODUCTION

Electrolysis of water using solar power to generate hydrogen is one of the most appealing strategies to produce green and sustainable fuel. 1-3 Unfortunately, two main factors are currently preventing it from finding a widespread use: (a) current electrocatalysts are designed using unsustainable materials such as platinum, palladium, and iridium, which are expensive and too scarce for sustainable widespread commercial usage, and (b) kinetics of hydrogen evolution reaction (HER) or oxygen evolution reaction (OER) for nonplatinum-group metal electrocatalysts are sluggish and exhibit a very high overpotential.² Fortunately, recent progress in HER and OER reactions has led to the development of a wide range of earth-abundant electrocatalysts (e.g., twodimensional materials including phosphides and oxyhydroxides), which are low in price and show similar or, sometimes, even higher efficiency compared to the noble metals.^{4–7}

Over the past few years, molybdenum disulfide (MoS_2) has emerged as a promising electrocatalyst for HER reactions due to its high density of active sites in the basal plane or at edge sites. ^{8,9} It is also highly stable in an acidic medium (based on the synthesis process) and has hydrogen binding energy similar to that of noble metals. In general, enhancing the electrocatalytic performance of MoS_2 catalysts can be achieved through three main approaches: (i) augmenting the quantity of exposed active sites, (ii) enhancing the electrical connectivity to these active sites, and (iii) boosting the intrinsic activity of individual active sites. These strategies have been widely

Received: May 29, 2024 Revised: July 26, 2024 Accepted: July 30, 2024 Published: August 2, 2024





explored to improve the ultimate HER activity of MoS₂. Similarly, nonprecious metal (such as nickel) electrocatalysts show outstanding OER activity because of the formation of either high-valent Ni=O or active Ni-O-O⁻ species. While all of these materials have been thoroughly studied, drawbacks such as complex material synthetic strategies and the lack of long-term stability limit their widespread use for electrocatalysis applications. All of these limitations motivate us to explore a stable, environmentally friendly, and large-scale electrocatalyst design capable of performing HER and OER as efficiently as platinum or iridium.

Introducing vacancies, increasing active-site populations, and phase adjustment can be promising strategies to enhance electrocatalytic efficiency. 13 For example, through a synergetic effect, carbon materials with hybridization to improve the charge transfer kinetics or heterostructures of two different materials (such as graphene and MoS_2) can provide ample catalytic active sites to enhance the catalytic activity. 4,14,15 In particular, growing the electrocatalyst on a conducting substrate with a binder-free method can be an efficient approach as the resulting structure can be used directly as a working electrocatalyst without further processing and, more importantly, excludes some of the components like Nafion, which covers surface-active sites resulting in lower catalytic activity. 16,17 Moreover, direct growth of the electrocatalyst on the conducting substrate also ensures the homogeneity of the catalyst compared to the conventional ultrasonication approach for manufacturing the electrocatalyst, which is key to improving the charge transport and access to the ample active sites throughout the electrocatalyst. 18

Finally, a suitable substrate can also help to maintain the structural integrity and chemical stability of the electrocatalyst throughout the process. Very recently, Lingappan et al. reported an approach based on conducting polymers such as polyaniline (PANI) to improve the interconnection between the CC substrate and electrocatalyst. 16 While this approach improves the overall structural integrity of the catalyst and improves the catalytic efficiency, the lack of a porous structure of the electrocatalyst limits transport throughout the material, and applying this approach over larger areas remains challenging. Scalability remains a key challenge to developing a low-cost, high-throughput technique for preparing composite or hybrid structured electrocatalysts with the desired qualities (e.g., high porosity, high electrical conductivity, and accessible surface area) by ensuring the full exposure of electrolytes, efficient charge transfer path, easy gas release, and synergetic effects.

Given these considerations, porous graphene sheets on carbon cloths (CC) can be an ideal substrate for an active electrocatalyst like nickel or MoS₂ due to their high electrical conductivity and well-aligned porous structure. Our group recently reported a rapid, efficient, and scalable approach to prepare porous graphene using photothermal pyrolysis (using xenon flash lamp (300–1100 nm)) of polymeric materials such as polybenzoxazine and polyacrylonitrile on various substrates such as CC, Kapton, and stainless steel in a few seconds. We highlight that this process can be utilized for large-scale porous, few layer graphene production.

Inspired by the key merits of PANI and photothermal pyrolysis, here, we report a new approach to designing durable and efficient electrocatalysts for the HER and the OER. PANI is deposited on the CC substrate using an electropolymerization process followed by photothermal pyrolysis to derive the

porous graphene directly grown on the CC substrate. PANI does not require additional thermal treatment for cross-linking before the carbonization, which makes the entire process of preparing porous graphene simple, fast, and cost-effective. Electrocatalysts for OER and HER are deposited on the PANIderived porous graphene-CC substrate, they are designated Ni (PANI-pf-CC@Ni) and MoS₂ (PANI-pf-CC@MoS₂). The incorporation of the porous graphene layer allows for coupling between the catalyst and support, which yields synergistic effects and creates a significantly enhanced performance compared with the single components. The PANI-pf-CC@Ni electrocatalyst showed an excellent OER performance with a low Tafel slope value of 35 mV/decade and the overpotential of 130 mV in a 1 M KOH electrolyte, while the PANI-pf-CC @MoS₂ electrocatalyst exhibits the HER performance with a low Tafel slope value of 40 mV/decade and an overpotential of 178 mV in a 0.5 M H₂SO₄ electrolyte at a current density of 10 mA/cm². We also incorporated the Ni species as a dopant into the MoS₂ structure to improve the HER activity. Raman spectroscopy, X-ray photoelectron spectroscopy (XPS), and density functional theory (DFT) studies were performed to gain insights into the mechanism of enhancement in the OER and HER reaction, revealing electrocatalytically active Ni hydroxide species at the Ni surface during the surfacereconstruction process responsible for the OER, whereas the structure of Ni doping in MoS₂ protects against the oxidation of sulfur atoms in the edge sites, which serve as active sites and consequently increases the HER activities. We further evaluated the HER performance of these electrocatalysts under commercial alkaline water electrolyzes (AWEs) conditions. Our study helps to understand the mechanism of a simple method of synthesizing porous electrocatalyst materials, emphasizing industrial requirements, which will provide new insights to explore the combination of commercial and laboratory investigations.

■ EXPERIMENTAL SECTION

Materials. Nickel(II) chloride hexahydrate (98%), boric acid (99.5%), aniline (99.5%), sodium molybdate dihydrate, thiourea, and concentrated sulfuric acid (\sim 98%) were purchased from Sigma-Aldrich. Potassium hydroxide (KOH) was obtained from Thermo Fisher Scientific (Waltham, MA, USA). Carbon cloth (80 cm × 130 cm, part no. CCP-122) was purchased from Fuel Cell Earth (Woburn, MA, USA). Stainless steel foil 316 was procured from MTI Corp. (Richmond, CA, USA). Unless otherwise noted, all materials were used without further purification. Ultrapure type I water (18.2 MΩ · cm) was used for all of the experiments.

Electrochemical Deposition of Polyaniline (PANI) on Carbon Cloth (CC). PANI was electrochemically deposited using a three-electrode system as described in previous reports. ²² Briefly, CC (5 cm × 5 cm) was used as the working electrode, stainless steel was used as a counter electrode, and Ag/AgCl was used as a reference electrode in a 0.3 M aniline and 1 M HCl electrolyte solution. The deposition was performed using a CHI660E electrochemical workstation (CH instruments Austin, TX) where a constant current density of 10 mA/cm² was applied for a desired duration ranging from 7 min to grow rod-like PANI. After deposition, PANI on CC was washed several times with water to remove the unreacted monomer and then dried overnight at room temperature under a fume hood and then at 100 °C for 1 h in an oven for further characterization.

Photothermal Pyrolysis of Polyaniline on Carbon Cloth (PANI-pf-CC). PANI on CC was photothermally pyrolyzed using a Novacentric Pulse forge 1300 xenon flash lamp system (Austin, Texas) under ambient conditions. Samples were placed at a stand-off distance of 10 mm from the lamp for processing. PANI on CC was first subjected to 10 pulses with a pulse voltage of 400 V, a pulse

length of 800 μ s, and a frequency of 1 Hz followed by 10 pulses with a pulse voltage of 600 V, a pulse length of 800 μ s, and a frequency of 1 Hz to completely transform the polymeric material into porous graphene. The carbon yield derived from PANI is calculated to be 50%, as evaluated by measuring the mass before and after photothermal processing.

Electrochemical Deposition of Nickel on PANI-pf-Graphene-CC (PANI-pf-GCC@Ni). Nickel was deposited on PANI-pf-GCC under galvanostatic conditions using a CHI660E electrochemical workstation (CH Instruments Austin, TX) in pulse mode, wherein the current was turned on for 0.5 s and turned off for 1 s. A piece of nickel foil served as the counter electrode, and Ag/AgCl was the reference electrode. The electrochemical bath was a mixture of 0.1 M nickel chloride and 0.2 M boric acid in deionized water. The electrochemical bath was stirred at 200 rpm by using a magnetic stir bar. The current density varied from 0.5-2.5 mA/cm². The total deposition time was varied from 15 s to 7 min. After the deposition was completed, PANI-pf-GCC@Ni was rinsed with deionized water and then dried at 100 °C on a hot plate for further characterization.

Preparation of Molybdenum Disulfide (MoS₂) on PANI-pf-GCC (PANI-pf-GCC@MoS₂). MoS₂ was grown on the PANI-pf-GCC using a hydrothermal method according to the previous report. 16 Sodium molybdate dihydrate (0.08 g, 0.3 mmol) and thiourea (0.126 g, 1.6 mmol) were dissolved in deionized water, (50 mL) and the resulting solution was transferred into a Teflon-lined autoclave. A piece of PANI-pf-GCC was placed into the mixture, and the autoclave was sealed and heated at 200 °C for 16 h. The obtained PANI-pf-GCC @MoS2 was removed, washed with excess water, and dried under vacuum for further characterization.

Electrochemical Deposition of Nickel on PANI-pf-GCC@ MoS₂ (PANI-pf-GCC@Ni-MoS₂). To assess the impact of Ni doping on MoS₂ catalysts, nickel was deposited on PANI-pf-GCC@MoS₂ under galvanostatic conditions using a CHI660E electrochemical workstation (CH instruments Austin, TX) in pulse mode, wherein the current was turned on for 0.5 s and turned off for 1 s. A piece of nickel foil served as the counter electrode, and Ag/AgCl was the reference electrode. The electrochemical bath was a mixture of 0.1 M nickel chloride and 0.2 M boric acid in deionized water. The electrochemical bath was stirred at 200 rpm using a magnetic stir bar. The current density was varied from 2.5 mA/cm². The total deposition time was varied from 15 s. After the deposition was completed, PANI-pf-GCC@Ni-MoS2 was rinsed with deionized water and then dried at 100 °C on a hot plate for further characterization.

Electrochemical Measurements and Calculations. A threeelectrode configuration was used for all electrochemical measurements in 1 M KOH for the OER and 0.5 M H₂SO₄ for the HER on a CH Instruments CHI660D electrochemical workstation at ambient temperature. As prepared PANI-pf-GCC@Ni (for the OER) and PANI-pf-GCC@MoS₂ (for the HER) support, graphite rod and Ag/ AgCl electrodes (saturated KCl) were used as working, counter, and reference electrodes, respectively. The active areas for the OER and HER supports were 2 cm² in which both sides of the carbon fiber participate in the electrochemical reactions. Linear sweep voltammetry (LSV) with a sweep rate of 5 mV/s was carried out at room temperature by using a three-electrode system with 1 M KOH (for the OER and HER) and 0.5 M H₂SO₄ (for the HER) electrolytes. A long-term stability test (current vs time) was carried out in 1 M KOH (for OER and HER) and 0.5 M H₂SO₄ (for HER) electrolytes using a three-electrode system with a fixed overpotential. A similar setup for LSV and long-term stability with 7.5 M KOH (30 wt %) at 80 °C was used to mimic commercial alkaline water electrolyze conditions. All potentials reported in this work are adjusted with the reversible hydrogen electrode (RHE). The equilibrium potential (E_0) for OER is 1.23 V vs RHE, so the overpotential is the potential difference between $E_{\rm RHE}$ and 1.23 V. Unless specified, the obtained LSV graphs were recorded without iR compensation. Electrochemical impedance spectroscopy (EIS) was performed using a CH Instruments CHI660D electrochemical workstation at ambient temperature with frequencies in the range of 100 kHz to 10 Hz at a voltage amplitude of 10 mV with potentials of 0.3 V for the OER and -1.5 V for the HER vs RHE.

The electrochemical surface area (ECSA) was calculated using cyclic voltammetry, which is used as a benchmark method for numerous electrocatalysts for the HER and the OER. In a non-Faradaic domain, several cyclic voltammetry (CV) scans were conducted at various scan rates (10, 20, 40, 60, 80, 100, and 120 mV/s). The mean disparity between anodic and cathodic charging current densities was graphed against the scan rate. The double-layer capacitance (C_{dl}) was determined by deriving the linear regression slope. $C_{\rm dl}$ was determined by deriving the slope of the linear regression. It is widely recognized that a catalyst with a higher C_{dl} value suggests a greater exposure of active sites relative to its active surface area. Tafel slope was calculated based on the following equation.

 $\eta = \text{aloglcurrent densityl} + \text{b}$

where " η " is the overpotential, "a" is the Tafel slope, and "b" is the exchange current density. Applying a linear fit to the Tafel equation allows for the determination of the Tafel slope. Each electrochemical experiment was run at least three times for reproducibility. All of the electrochemical deposition and measurement were carried out under

Microscopy and Spectroscopy. Field emission scanning electron microscopy (SEM) measurements were carried out on a FEI Magellan 400 FESEM at an accelerating voltage of 3 kV and a current of 15 pA. X-Ray diffraction (XRD) patterns were obtained with a Panalytical X-ray diffractometer with 1.5418 Å Cu K_α radiation. X-Ray photoelectron (XPS) analysis was performed using a Physical Electronics VersaProbe III instrument equipped with a monochromatic Al K_{α} X-ray source ($h\nu = 1,486.6$ eV) and a concentric hemispherical analyzer. Charge neutralization was performed using both low-energy electrons (<5 eV) and argon ions. The binding energy axis was calibrated using sputter-cleaned Cu (Cu $2p_{3/2} = 932.6$ eV, Cu $3p_{3/2} = 75.1$ eV) and Au foils (Au $4f_{7/2} = 83.9$ eV). Peaks were charged as referenced to the sp² band in the carbon 1s spectra at 284.5 eV. Measurements were made at a takeoff angle of 45° with respect to the sample surface plane. These specifications resulted in a typical sampling depth of 3-6 nm (95% of the signal originated from this depth or shallower). Quantification was done using instrumental relative sensitivity factors (RSFs) that account for the X-ray crosssection and inelastic mean free path of the electrons. Major elements (>5 atom %) on homogeneous samples tend to have standard deviations of <3%, while minor elements can be significantly higher. The analysis size was \sim 200 μ m in diameter. CasaXPS software was used to analyze the spectra.

A DXR Raman microscope from Thermo Fisher Scientific was used for an ex situ Raman spectrum over a range of 100-3500 cm⁻¹ with a resolution of 5.3-8.8 cm⁻¹, using a 20× objective backscattering configuration. Three different spots of each sample were obtained by using a focused 633 nm laser (power = 5 mW) on a 1.6 μ m spot size to avoid sample damage.

First-Principle Calculations. Spin-polarized, periodic DFT calculations were performed with the VASP package (Version 6.1.2), 23,24 using the PBE exchange-correlation functional and a plane-wave basis set with a kinetic energy cutoff of 400 eV for the valence electrons. The PAW method was utilized for treating core electrons, with PAW potentials selected to include 1 valence electron for H, 4 for C, 5 for N, 6 for O, 6 for S, 10 for Ni, and 6 for Mo, respectively. A 3 × 3 × 1 K-point grid was used for sampling the reciprocal space in the OER system. Structure optimization converged to below a force threshold of $0.02~{\rm eV/\AA}$ for the OER system. The vibrational analysis was conducted by computing the second-order derivatives of the total energy with respect to the position of the ions using the central finite difference with a step size of 0.015 Å. The stop criterion for the electronic self-consistent loop was set to be 10⁻⁶ eV for the vibrational calculations.

RESULTS AND DISCUSSION

Characterization of the PANI Composite and Effect of Photothermal Pyrolysis. The CC substrate was functionalized with PANI by oxidative electropolymerization of aniline

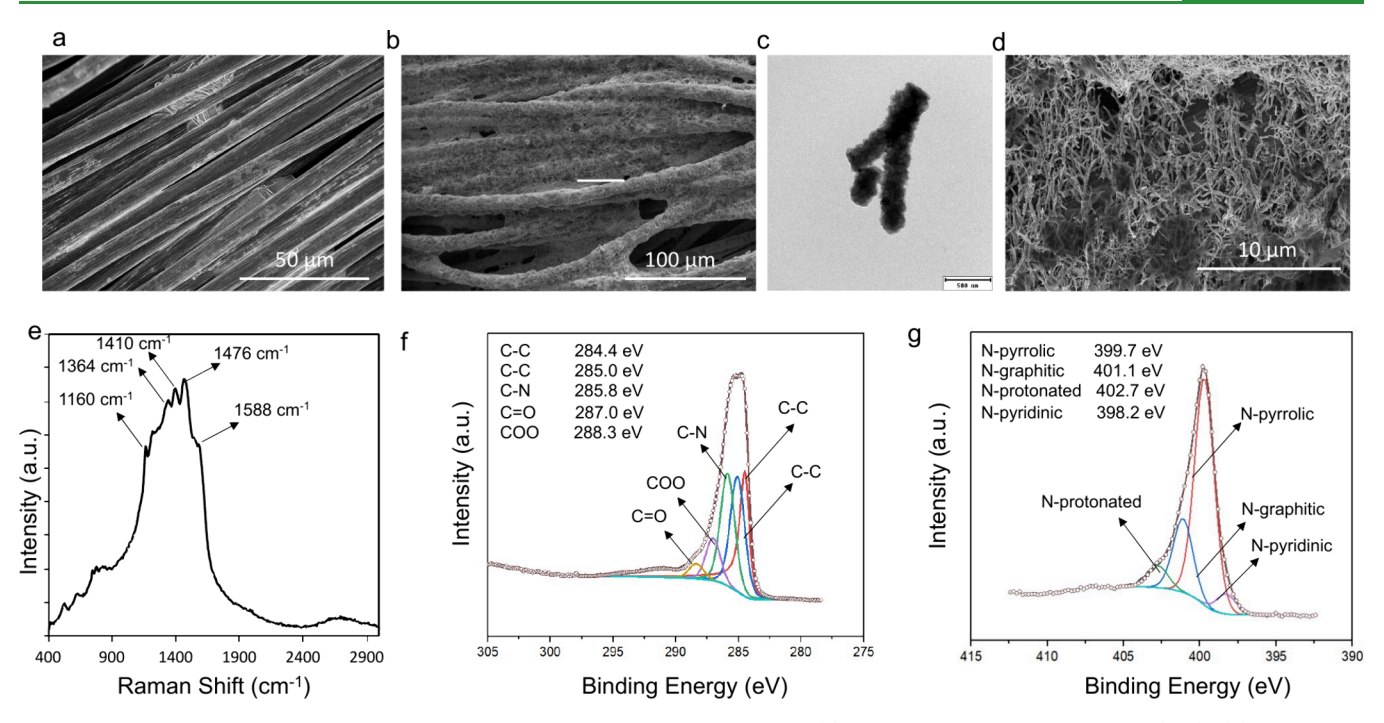


Figure 1. Surface morphology and spectroscopic characterization of PANI composite. (a) SEM image of bare carbon cloth (CC); (b) SEM image showing the overall distribution of PANI on CC; (c) TEM image showing fibrous PANI. The scale bar is 500 nm; (d) SEM image showing fibrous PANI distribution; (e) Raman spectroscopy of PANI composite taken at 633 nm wavelength; (f) high-resolution C 1s XPS spectra; and (g) highresolution N 1s XPS spectra.

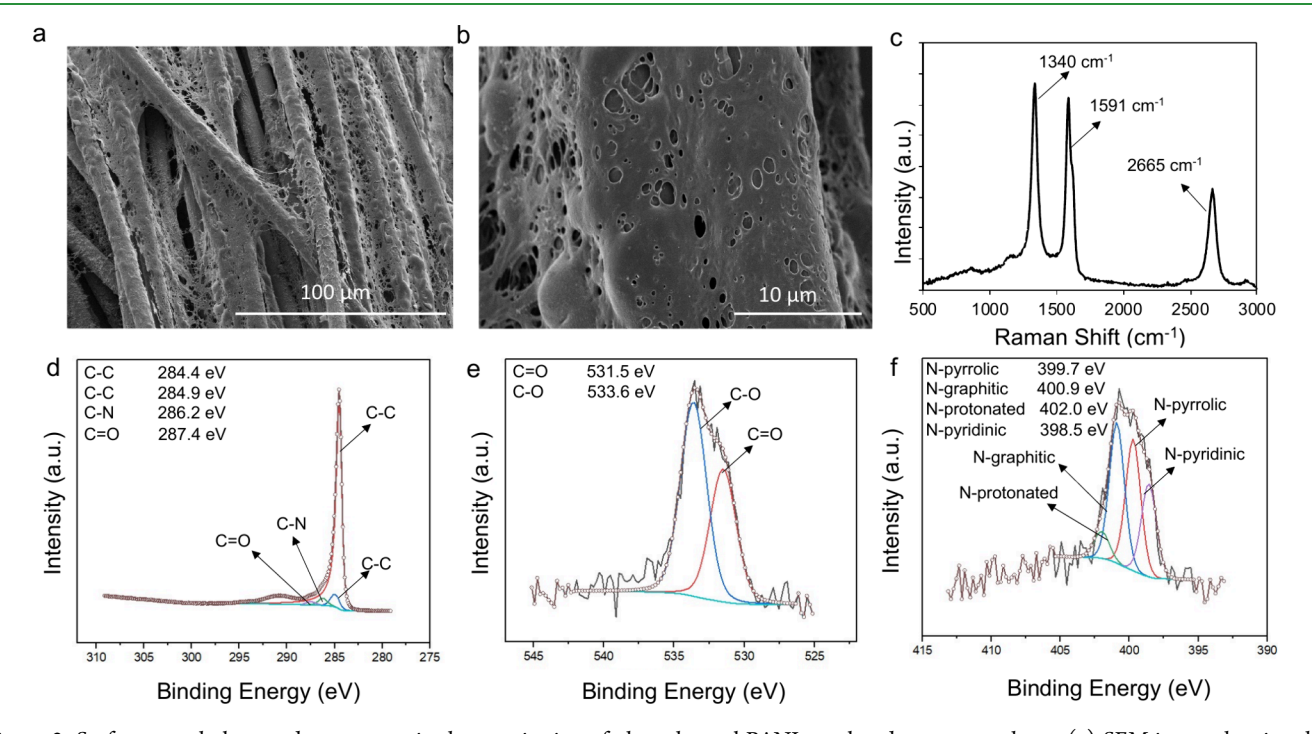


Figure 2. Surface morphology and spectroscopic characterization of photothermal PANI-pyrolyzed porous graphene. (a) SEM image showing the homogeneous photothermal pyrolysis of PANI on CC; (b) zoom-in SEM image of porous graphene; (c) Raman spectroscopy of porous graphene taken at a 633 nm wavelength; (d) high-resolution C 1s XPS spectra; (e) high-resolution O 1s XPS spectra; and (f) high-resolution N 1s XPS spectra.

in an acidic medium. After electrochemically functionalizing PANI on CC, a black CC substrate turned into a green color, indicating a successful coating of PANI in the emeraldine salt form (Figure S1). PANI deposition was characterized by scanning electron microscopy (SEM) (Figure 1a,b) and transmission electron microscopy (TEM) (Figure 1c). The

SEM results revealed that the PANI layers are homogeneously covering (Figure 1b) the CC fiber surface possibly owing to the $\pi - \pi$ interaction. ²⁵ The uniform distribution of PANI will ensure the uniformity of graphene conversion after pyrolysis, which is important to strengthen the interaction between the electrocatalysts and substrate. The high-magnification SEM

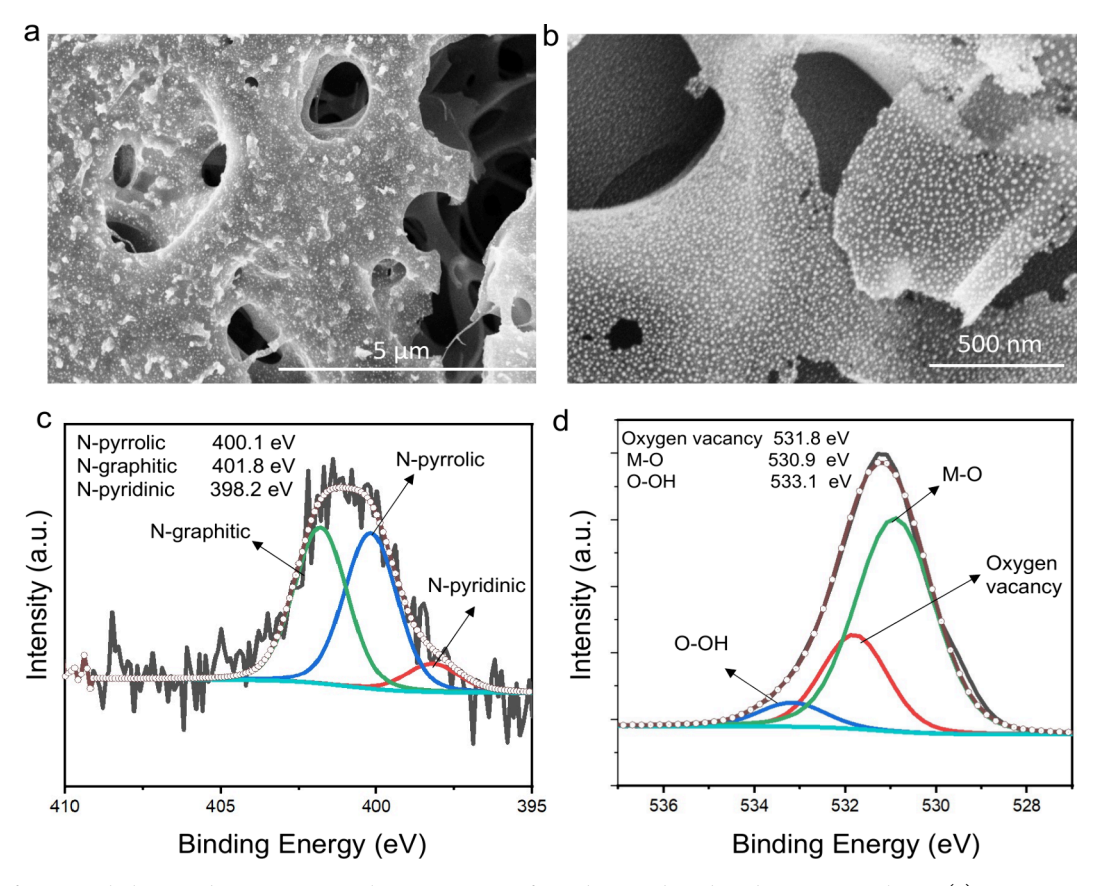


Figure 3. Surface morphology and spectroscopic characterization of Ni deposited N-doped porous graphene. (a) SEM image showing the homogeneous distribution of Ni; (b) Zoom-in SEM image of Ni species; (c) high-resolution N 1s XPS spectra; and (d) high-resolution O 1s XPS spectra.

image of PANI reveals a nanofiber structure without any agglomeration (Figure 1d). The functionalization of PANI was studied by Raman spectroscopy. The characteristic peaks at 1588, 1476, 1364, and 1160 cm⁻¹ correspond to the C-C, C-N, and C-N+ radical cation stretching and in-plane C-H bending of PANI (Figure 1e).26 The survey spectrum of XPS analysis (Figure S2) further confirmed the presence of carbon (81.8 at %), oxygen (2.8 at %), and nitrogen (11.4 at %), respectively. As resolved in the high-resolution deconvoluted XPS data in Figure 1f, the C 1s spectra with binding energies of 284.4, 285.0, 285.8, 287.0, and 288.3 eV can be assigned to the quinoid structure of the compound, aliphatic C-C, C-N, C=O, and COO, respectively. $^{27-29}$ The fitted high-resolution XPS of N 1s (Figure 1g) at the binding energies of 399.7, 401.1, 402.7, and 398.2 eV are the characteristic peaks of pyrrolic-N, graphitic-N, protonated graphitic-N, and pyridinic-N, respectively.³⁰ Nitrogen species in PANI will play a pivotal role in preparing porous nitrogen-doped graphene due to its high nitrogen-to-carbon ratio that can be maintained even after pyrolysis without using a nitrogen atmosphere. The presence of those nitrogen species will also influence the interconnection with the electrocatalysts.

After PANI functionalization on CC, photothermal pyrolysis using a xenon flash lamp was carried out at different irradiation energies to obtain the porous graphene. Two steps of the pyrolysis process were used to obtain the porous graphene, first a low-energy cycle of 1.80 J/cm² per pulse was used to remove all the small organic hybrids, followed by a slightly higher energy cycle of 5.95J/cm² per pulse was used to completely convert PANI to porous graphene. In the pulse forge, the

irradiated energies were utilized as a temperature source that reached over 2000 °C in a few seconds (as predicted by a simulation; Figure S3), which was done to remove the organic moieties. This method is more time effective as compared to a slow conventional tube furnace, which takes more than 6 h to reach 800 °C. Furthermore, by controlling the pulse energy in photothermal pyrolysis, the desired morphology and chemical composition can be determined. The high-resolution SEM images (Figure 2a,b) showed an interconnected porous architecture from PANI with pore ranges of several nanometers. The homogeneous distribution of the porous architecture further suggested that the pulse forge photothermal process is very uniform. To clarify the nature of this porous framework, Raman spectroscopy and XPS analysis were carried out. The characteristic Raman peaks at 1340, 1591, and 2665 cm⁻¹ represent the disordered D band, graphitic carbon-related G band, and second order of D bands (2D band), respectively, confirming the successful transformation of PANI to graphene (Figure 2c).³¹ Finally, the fitted XPS binding energies of 284.4, 286.2, and 287.4 eV can be assigned to (C-C) sp², C-N, and C=O, respectively, which further corroborate that the PANI transform porous architecture has a few layer graphene structure (Figure 2d).31 A potential explanation can be derived based on the energy dependence and magnitude of the pulse energy, which generates an elevated temperature and forces PANI to rearrange a rod-like configuration to a network-like porous graphene structure. It is important to note that a small amount (C-C) sp³ at the binding energy of 284.9 eV was also detected in the XPS peak fitting because of aliphatic carbon. This suggests that the carbon structure is not completely

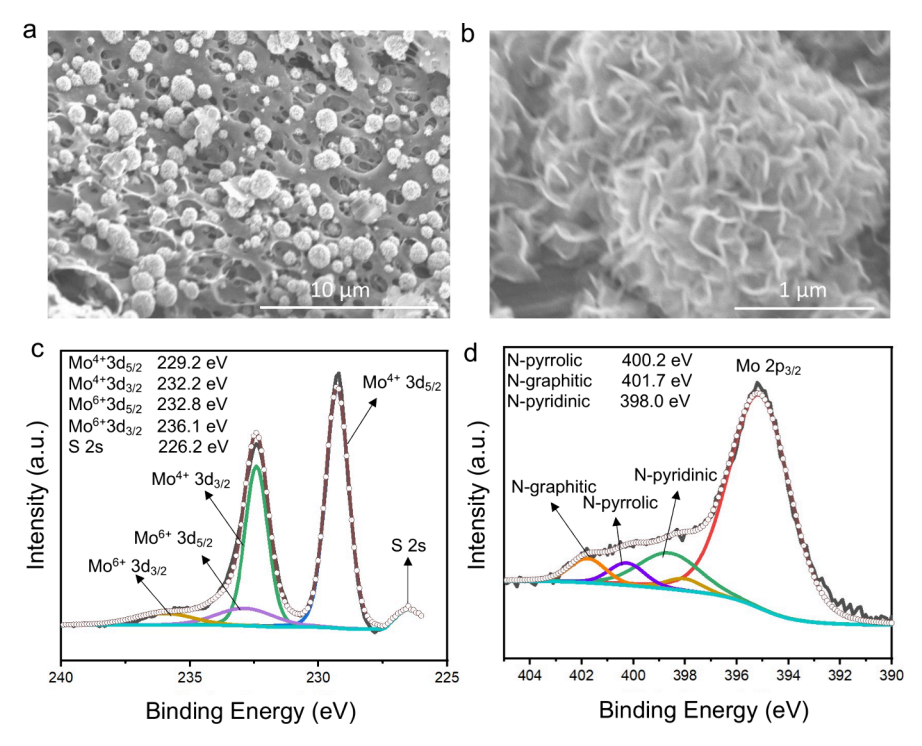


Figure 4. Surface morphology and spectroscopic characterization of MoS_2 deposited N-doped porous graphene. (a) SEM image showing the homogeneous distribution of MoS_2 ; (b) zoom-in SEM image of MoS_2 flower; (c) high-resolution Mo 3d XPS spectra; and (d) high-resolution N 1s XPS spectra.

ordered and defects are present in the graphitic moieties. Furthermore, the number of heteroatoms detected by XPS (Figure S4) after photothermal pyrolysis was significantly decreased to oxygen (1 a%) and nitrogen (1 a%). This is not a very surprising result considering that the obtained temperature of our process was over 1000 °C, which removes most heteroatoms in the system. The high-resolution XPS of O 1s revealed the presence of surface functional groups of C=O and C-O with binding energies of 531.5 and 533.6 eV, respectively (Figure 2e). This can be attributed to functionalization within the carbon structure. Our photothermal pyrolyzed graphene exhibits observable defects, as indicated by the prominent "D" peak in Raman spectroscopy (Figure 2c). These functional defects, commonly oxygen-related, are expected, given the imperfect nature of our carbon framework. This observation aligns with the findings in the literature. 27,32 The N 1s spectrum (Figure 2f) also revealed the presence of pyrrolic-N, graphitic-N, protonated graphitic-N, and pyridinic-N, respectively. Both surface functional groups and N doping in the graphene moiety will not only help the wettability of the electrocatalyst by the electrolyte but also provide anchoring sites for MoS₂ and Ni. Thus, both microscopy and spectroscopy results clearly demonstrated that the obtained porous architecture material is nitrogen- and oxygen-doped graphene that has grown on the CC without any binder and can be used to construct both Ni and MoS2 for the water-splitting experiments.

Construction and Structural Characterization of PANI-pf-GC@Ni. The OER electrocatalytic activities in this work were investigated using Ni on an as-synthesized porous graphene substrate. Before the determination of the OER performance of the electrocatalyst, it is essential to understand the morphology and surface composition of the material. Ni was electrochemically deposited on the PANI-pf-

GCC using the three-electrode pulse mode "on" and "off" method in which at a particular current density of Ni atoms will be at a nucleation state during the current "on" step. The alternating "on" and "off" steps help us to restrict the growth stage of Ni deposition. 33,34 In this process, there will be a high probability of forming large aggregates of nickel particles, similar to a Ni plating process. The aggregation of Ni leads to a lower electrocatalysis performance, which is not desired, and it is best to optimize the particle growth to avoid aggregation. To investigate how and why the current density and time duration in the pulse mode affect the particle growth, a series of depositions were carried out with a range of current densities between 5 and 15 mA/cm² and duration times from 15 to 420 s, the corresponding SEM images showed in Figure S5. These results help us in shortlisting the most probable current densities and timing to get the least aggregated particle. It was noticed that the 5 mA/cm² current density with 60 s deposition time showed the least aggregated particle area on the substrate (Figure S6). Thus, the deposition time and current density were further reduced to 15 s and 2.5 mA/cm², respectively, which resulted in a homogeneous deposition of nickel particles without covering the pores and with minimal aggregation. The high-resolution SEM (Figure 3a,b) also suggested that the growth particle size is around 15.72 nm with a standard deviation of 3.08 nm (Figure S7 for size distribution). We hypothesize that, in the pulse mode deposition process, when the current density is stabilized, the growth stage begins leading to aggregation. This is also supported by the SEM images (Figure S5), where large aggregation occurs at a longer time. All the electron microscope results using these conditions confirm the successful deposition with minimal Ni aggregation on PANIpf-GCC and the successful synthesis of the PANI-pf-GCC@Ni catalyst with optimized morphology. XPS was further

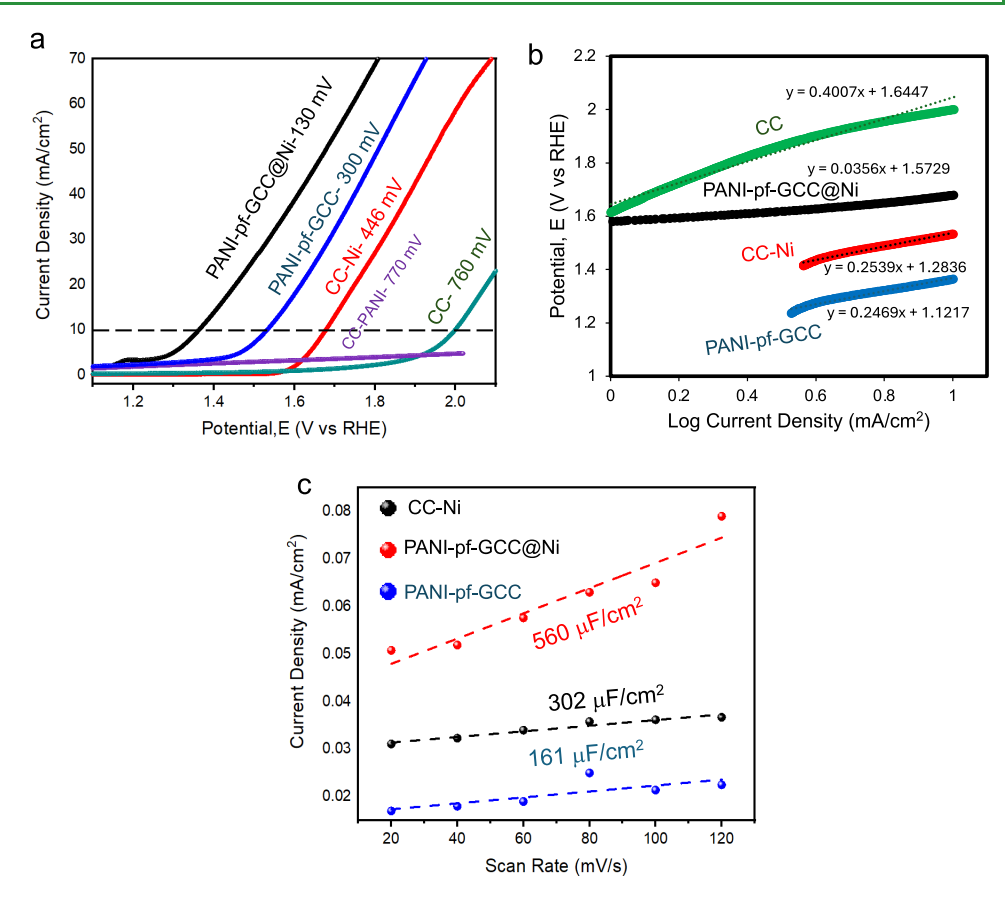


Figure 5. OER performance of synthesized catalysts in a 1 M KOH electrolyte. "N-Doped graphene" without any catalyst is used as a reference for comparison. (a) Polarization graph of different catalysts at a scan rate of 5 mV/s, where the *y* axis was normalized based on the geometric surface area; (b) corresponding Tafel plots, and (c) electrochemical surface area.

performed to understand the surface chemical composition of PANI-pf-GCC@Ni. The full survey XPS spectrum of the existence of C, O, N, and Ni elements is shown in Figure S8. The XPS spectrum of Ni 2p reveals (Figure S9) two spinorbit doublets at binding energy values of 857.2 and 873.8 eV, exhibiting a spin-energy separation of 16.0 eV, indicative of the Ni $2p_{3/2}$ and Ni $2p_{1/2}$ components, respectively.³⁵ The peak positions at 879.3 and 860.3 eV correspond to satellite peaks of Ni 2p_{1/2} and Ni 2p_{3/2}, respectively. 36,37 The presence of satellite peaks suggests that Ni²⁺ predominates as the major component.³⁸ The characteristic peak at 857.2 eV in binding energy signifies the presence of NiOOH, indicating that surface Ni species are in an oxidized state. This is unsurprising given that pure metallic Ni is highly susceptible to oxidation, even without the application of any potential.³⁹ The N 1s spectrum (Figure 3c) displayed three characteristic peaks at the binding energy of 398.2, 400.1, and 401.8 eV, respectively, because of the pyridinic-N, pyrrolic-N, and graphitic-N. The high-resolution O 1s spectra (Figure 3d) suggested three distinct peaks at the binding energies of 531.8, 530.9, and 533.1 eV, respectively. 40 The peak at the binding energy of 531.8 eV indicated the oxygen vacancies, whereas 530.9 eV can be associated with hydroxyl species of hydroxides. 41 The peak at the binding energies of 533.1 eV results from the hydroxyl species that evolved due to the water and oxygen vacancy interaction. 42 These oxygen defect peaks are important in enhancing the electrocatalytic activity. Further, the oxygen vacancies and OH groups contribute free electrons, thereby increasing the charge carrier concentration at the interface,

which directly affects conductivity. The presence of surfaceadsorbed O2/OH of PANI-pf-GCC@Ni qualitatively suggests the availability of more accessible catalytic active sites. Consequently, accelerated OER kinetics are expected on the surface of the PANI-pf-GCC@Ni catalyst. XPS primarily investigates the surface layer of a sample, typically within 10 nm. However, Raman spectroscopy offers insights into the bulk structure and properties, providing a more comprehensive understanding. The Raman spectra (Figure S10) depict notable characteristic features, including peaks at around 1329 and 1580 cm⁻¹, attributed to the D and G bands of graphene, respectively, alongside the 2D band at 2657 cm⁻¹. The intensity ratio of the D and G peaks (0.87) suggests the presence of multilayer graphene with relatively fewer defects and disordered carbon, which is consistent with our XPS analysis.⁴³ Moreover, the Raman spectrum reveals distinct peaks corresponding to the oxidized form of Ni at 914 cm⁻¹ (2LO). Additionally, a peak at 368 cm⁻¹ is likely associated with the E_o vibration mode of the Ni-OH lattice, while peaks at 466 cm⁻¹ and a shoulder around 600 cm⁻¹ indicate stretching vibration modes of Ni-O nanostructures. 44,45

Construction and Structural Characterization of PANI-pf-GCC@MoS₂. The HER electrocatalytic activity was investigated by using MoS₂ on the as-synthesized porous graphene substrate. The SEM image (Figure 4a) showed that the MoS₂ was grown on the porous graphene substrate without destroying the pores. This is particularly important because we are speculating that covering the entire pores will decrease the diffusion during the electrochemical process. Therefore,

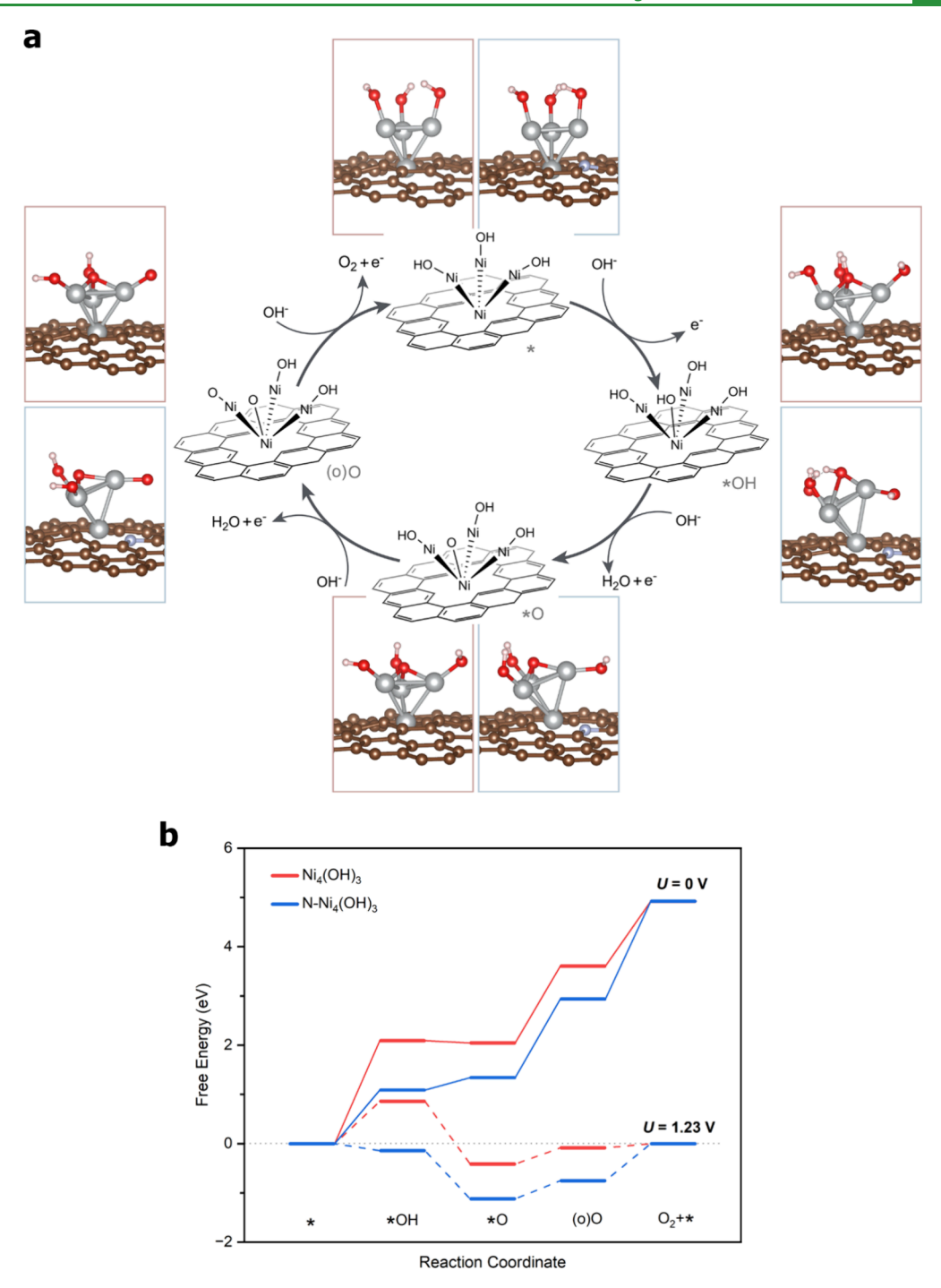


Figure 6. Mechanisms and free-energy profiles of the OER process. (a) The schematic illustrates the nickel hydroxide cluster considered in the DFT calculations, showing the reaction mechanisms involving *, *OH, *O, and (o)O, where the asterisk denotes the active site and (o) indicates an oxidized active site (see text); (b) free-energy diagrams for the OER process under alkaline conditions (pH = 14), showing the condition with an applied potential of U = 0 (solid lines) and 1.23 V (dashed lines) relative to the Reversible Hydrogen Electrode (RHE). The red borders in panel a and red curves in panel b correspond to structures on an undoped graphene substrate, while the blue color corresponds to structures on a nitrogen-doped graphene substrate.

controlling the hydrothermal synthesis time is important. We optimized the synthesis time comparing 24, 12, and 16 h and by monitoring the MoS_2 growth using SEM images (Figure S11). It was found that the 16 h hydrothermal process had the best growth of MoS_2 without destroying the porous structure of the graphene substrate. The high-resolution SEM image (Figure 4b) further indicates that the grown MoS_2 on PANI-pf-GCC has a flake-like structure with small edges. This is

because of the coordination interaction during the hydrothermal synthesis between the molybdenum precursor and nitrogen species in the porous graphene. Raman spectroscopy (Figure S12) was used to understand the bulk structure and properties of PANI-pf-GCC@MoS₂. The characteristic Raman peaks of MoS₂ at 633 nm wavelength are dominated by 378, 410, and 455 cm⁻¹ because of in-plane $\rm E^1_{2g}$ mode, out-of-plane $\rm A_{1g}$ mode, and second-order Raman scattering 2LA(M)

mode. 46 Two new peaks of 190 and 226 cm⁻¹ can be assigned to the formation of 1T phase MoS₂.⁴⁷ A small peak in the region of 340–350 cm⁻¹ also suggested the sulfur vacancies in the sample. 16 Peaks at 1342 and 1608 cm⁻¹ are associated with the D and G bands of the mesoporous graphene. Notably, no oxysulfide peak at 440 cm⁻¹ was observed during the synthesis process. 48 Chemical surface analysis of PANI-pf-GCC@ MoS₂ was further performed using XPS. A Mo 3d_{5/2} binding energy of 229.2 eV represents Mo⁴⁺ in 2H-MoS₂, and a Mo 3d^{5/2} binding energy of 232.8 eV is characteristic of Mo⁶⁺ such as in molybdenum trioxide (MoO₃) (Figure 4c).⁴⁶ Combined XPS survey and high-resolution data further suggested that the S²⁻/ Mo⁴⁺ ratio for MoS₂ is not 2 but rather 1.35, indicating the possible sulfur vacancies in the sample, which is also supported by Raman spectroscopy. In our sample, S 2p_{3/2} peaks associated with sulfide in MoS₂ are observed at the binding energy of 162.1 eV (Figure S13).⁴⁶ Furthermore, we observed an overlap between the Mo 3p and N 1s binding energies. Interestingly, the N 1s peak (Figure 4d) does not show any protonated nitrogen species, instead a peak at the binding energy of 400.2 eV can be assigned to molybdenum-nitrogen coordination bonding. 16,49 Thus, this supports our hypothesis that the coordination bonding interaction between MoS2 and the porous N-doped graphene helps to grow the flake-like structure with small edges. 50 The N 1s spectrum (Figure 4d) also displayed the graphitic-N and pyridinic-N peaks at the binding energies of 398.0 and 401.7 eV, respectively. Notably, the C 1s peak (Figure S14) at a binding energy of 284.4 eV was assigned to sp² C-C, whereas 284.9 eV was for sp³ C-C, which indicates the retention of the graphitic structure with a defect in the PANI-pf-GCC@MoS₂ sample.

Oxygen Evolution Reaction (OER): Experimental, Spectroscopic, and Theoretical Analysis. The electrocatalytic OER activity was tested using a PANI-pf-GCC@Ni as the working electrode in a typical three-electrode system with a 1 M KOH aqueous electrolyte. First, the polarization curves (I vs V) were obtained using linear sweep voltammetry, which shows a fast kinetics wherein a required potential to reach 10 mA/cm² was found to be 1.36 V (vs RHE) (Figure 5a) and the corresponding Tafel slope value was 35 mV/decade (Figure 5b). The overpotential of 130 mV is much lower than those reported previously for Ni in alkaline electrolytes (e.g., overpotentials of 300, 290, and 230 mV at the current density of 10 mA/cm²).^{51,52} To understand the impact of Ni and the existence of active sites of PANI-pf-GCC@Ni, polarization performance evaluation and Tafel slope value calculations were carried out in three control samples, namely, CC-PANI, CC-Ni, and PANI-pf-GCC. The polarization graphs showed that the overpotentials of CC-PANI, CC-Ni, and PANI-pf-GCC were 770, 446, and 300 mV, respectively (Figure 5a). This increase in overpotential suggests that the incorporation of Ni in graphene favored the OER process. Increased Tafel slope values (246 mV/decade for PANI-pf-GCC and 253 mV/ decade for CC-Ni) (Figure 5b) were further observed for all the control samples, indicating less availability of active sites, as well as the necessity of both the porous structure and Ni simultaneously to achieve efficient oxygen evolution compared to the PANI-pf-GCC@Ni sample. Generally, good electrocatalytic performance implies a good electron transfer process between the electrocatalyst and electrolytes. To investigate how the electron transfer process affects the electrochemical properties, EIS was carried out in all the samples. The Nyquist plot (Figure S15) suggested that the PANI-pf-GCC@Ni sample has a lower charge transfer resistance (R_{ct}) value (8 Ω) compared to CC-Ni (28 Ω) and PANI-pf-GCC (22 Ω). These results indicated that the porous structure and Ni incorporation in the graphene matrix promoted electron transfer. Electrochemical surface area (ECSA) was further measured for all of the samples to calculate the number of electrochemically active sites (Figure 5c). ECSA was calculated by measuring the double-layer capacitance with different scan rates in the non-Faradaic zone as they are proportional to the ECSA. 53,54 The larger capacitance value (560 μ F/cm²) was obtained for the PANI-pf-GCC@Ni sample compared to CC-Ni (302 μ F/cm²) and the PANI-pf-GCC (161 μ F/cm²) samples. These values suggest that the nickel species in the graphene enhanced the intrinsic OER activities, which is consistent with the measured Tafel slope value. Based on the electrochemical measurement, we speculate that the higher OER performance is because of (a) the Ni hydroxide species formation in the OER process that enhanced the catalytic activity of PANI-pf-GCC@Ni sample; and (b) a more efficient charge transfer between electrolyte and electrode due to the Ni species, the mesoporous structure, and the beneficial synergy with N-doped graphene support.

To gain further insights into the nature of plausible active sites and OER mechanisms on these materials, DFT calculations were conducted to compare nickel clusters supported on graphene with and without nitrogen doping. Since we did not detect any Ni-C peaks in the XPS spectrum nor Ni-N-C single-atom images (although not quantified) in the high-resolution TEM, we consider a Ni₄(OH)₃ cluster⁵⁵ instead of Ni-C or Ni-N-C single-atom sites (see Figure 6a). To accommodate the nickel cluster, we removed two C atoms from the graphene substrate to create a divacancy defect⁵⁶ and substituted N for one of the remaining nearestneighbor C atoms to create the nitrogen-doped structure. The hollow site of the Ni hydroxide cluster was considered as the catalytically active center.⁵⁵ Generally, the standard OER mechanism in alkaline media consists of four coupled hydroxide-electron transfer steps on surface metal sites, 57,7 involving four different surface intermediates: *OH, *O, *OOH, and *OO. The catalytic cycle starts with a hydroxide ion attacking the center Ni atom in the first oxidation step, generating *OH. Another OH⁻ then abstracts the proton from *OH to form water and facilitate the second oxidation step. However, rather than the subsequent nucleophilic attack by another OH- to form *OOH, we found that the third oxidation step is preferred, which forms another water molecule by abstracting a proton from a nearby Ni-OH group, leading to an oxidized active-site ensemble indicated in Figure 6 as (o)O. As a result, the last oxidation step in the OER process here involves formally the dissociation of a fourth OH ion, regenerating the neighboring Ni-OH and forming *OO, which desorbs to complete the catalytic cycle. Given the alkaline environment (pH = 14), the question arises as to whether the nickel cluster should exist as Ni₄(OH)₃ or rather Ni_4O_3 . To a first approximation,⁵⁸ however, the reaction $Ni_4(OH)_3 \rightarrow Ni_4O_3 + H^+ + e^-$ is not pH-dependent under the same applied potential relative to RHE and the comparison of the stabilities of the two phases indicates that Ni₄(OH)₃ prevails at applied potentials until at least U = 1.4 V relative to RHE. Figure 6b shows the calculated free-energy profiles of the OER process. For the undoped active-site model, Ni₄(OH)₃, the potential-determining step is the first hydroxide-electron transfer to form the *OH state, with a

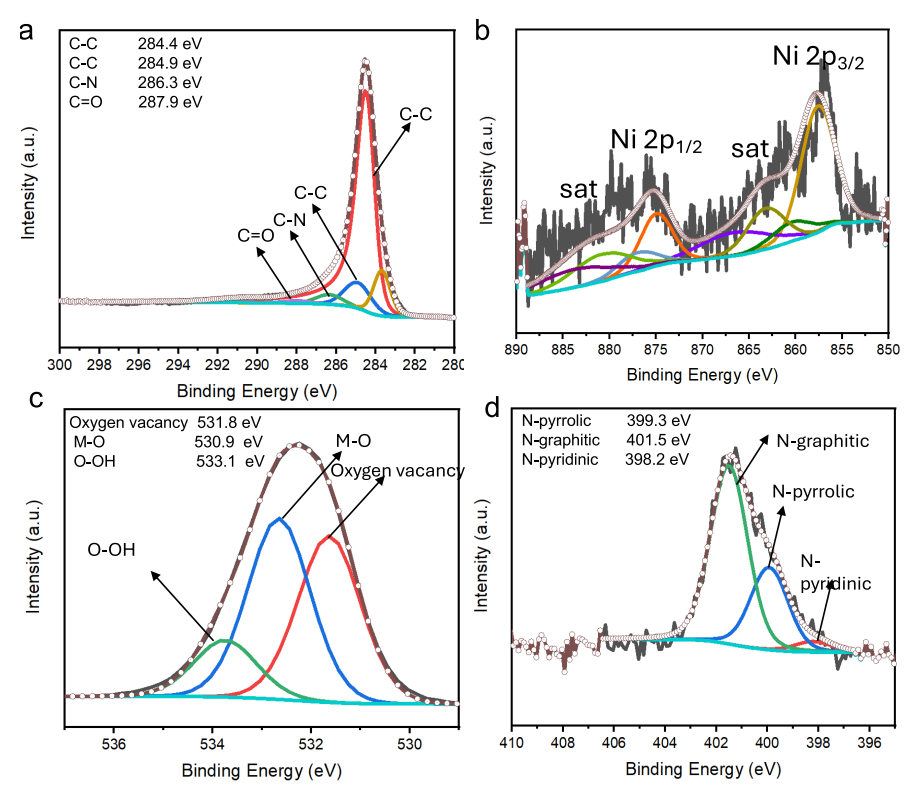


Figure 7. High-resolution XPS of post-OER-PANI-pf-GCC@Ni of (a) C 1s; (b) Ni 2p; (c) O 1s; and (d) N 1s.

free-energy cost of 2.09 eV at U = 0, which lowers to 0.86 eV under an applied potential of U = 1.23 V. For the N-doped active-site model, N-Ni₄(OH)₃, the highest reaction free energy occurs at the last step of O_2 formation, with $\Delta G = 1.98$ eV that further decreases to 0.75 eV under an applied potential of U = 1.23 V.

To validate the DFT calculations, XPS studies were further carried out in C 1s, Ni 2p, O 1s, and N 1s elements in the post-OER sample (Figure 7a-d) to understand the mechanism behind the enhanced OER activity. Following the OER process, the samples underwent LSV multiple times before being subjected to XPS analysis. In the resulting highresolution O 1s XPS spectra (Figure 7c), three discernible peaks emerged at 530.9, 531.8, and 533.1 eV, corresponding to lattice oxygen (M-O), oxygen vacancies, and hydroxyl groups, respectively. 59,41,16 Interestingly, the atomic percentage of oxygen increased significantly from 24 at % in the pristine sample to 36 at % in the post-OER samples. The rise in oxygen content can be attributed to the amplified formation of nickeloxo layers, as evidenced by the peaks at a binding energy of 857.6 eV in the Ni 2p XPS spectra. While these peaks were indeed discernible in the pristine material, their presence was relatively limited compared to the post-OER samples, indicating a notable increase in the formation of nickel-oxo species following the OER process. Additionally, the formation of oxidized C=O and C-O species on the defective graphene surface contributes to this observed increase in oxygen content. 60,61 The high-resolution Ni 2p peak identification also provides some insight into the variations in oxidation of the Ni surface. Similar to the pristine PANI-pf-GCC@Ni sample, the consistent Ni atomic percentage suggests that a portion of the catalyst's surface likely participated in the formation of Ni hydroxide/oxyhydroxy species during the OER process. Additionally, it is worth noting that, while a

weak shakeup peak centered around 852.1 eV is indicative of Ni's metallic state, it is not initially detected in the pristine form (Figure S9), post-OER (Figure 7b) reveals a minimal amount of metallic Ni at 852.1 eV. However, its significantly low percentage atomic area (0.09) means this can be disregarded. Consequently, there is no evidence of metal agglomeration during the catalyst preparation process or during the OER. This suggests that the catalyst remains stable without forming larger metal structures. Such stability is desirable in catalyst design, as it ensures consistent performance over time. Further, the binding energies of C 1s (binding energies of the fitted peaks are 284.4 eV for C-C sp², 284.9 eV for C-C sp³, 286.3 eV for C-N/C-O, 287.9 eV for C=O, and 283.6 for carbide) and N 1s (binding energies of the fitted peaks are 398.2 eV for pyridinic, 399.3 eV for pyrrolic, and 401.5 eV for graphitic) spectra between pristine and post-OER samples (Figure 7a,d) indicate that the graphene structure is still intact after OER with nitrogen and metal coordination. After conducting the OER LSV test, we proceeded with further characterization of the materials by utilizing Raman spectroscopy (Figure S16). Upon comparison with the pristine materials prior to the OER process, the Raman spectrum exhibits notable features, including a pronounced peak at 368 cm⁻¹ attributed to the E_g vibration mode of the Ni-OH lattice, and another at 634 cm⁻¹ indicative of stretching vibration modes of Ni–O nanostructures. 62,63 This observation suggests the formation of additional nickel-oxo layers within the graphene moiety, a finding that aligns with our XPS and DFT analysis.

Stability is a crucial aspect of water-splitting electrocatalysts, significantly impacting their viability for large-scale electrolyzers. A durability test was conducted using chronoamperometry for 60 h at a fixed potential vs RHE in 1.0 M KOH, as illustrated in Figure S17a,b. The electrocatalyst demonstrated

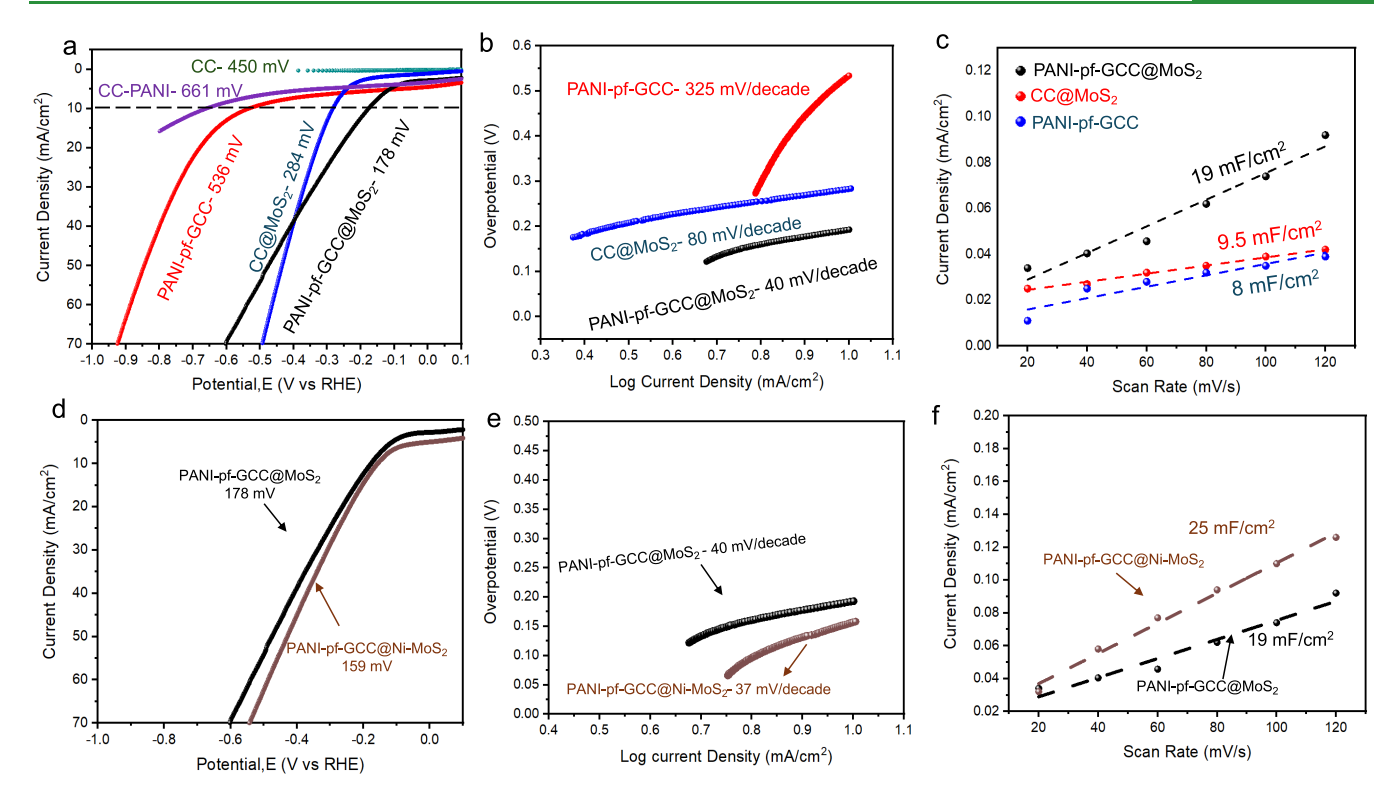


Figure 8. HER performance of synthesized catalysts in a $0.5 \text{ M H}_2\text{SO}_4\text{electrolyte}$. "N-Doped graphene" without any catalyst was used as a reference for comparison. (a) Polarization graph of different catalysts at a scan rate of 5 mV/s, where the y axis was normalized based on the geometric surface area; (b) corresponding Tafel plots; (c) electrochemical surface area; (d) HER performance comparison between PANI-pf-GCC@ MoS₂ and PANI-pf-GCC@Ni-MoS₂ samples in a $0.5 \text{ M H}_2\text{SO}_4$ electrolyte. Polarization graphs were made using a scan rate of 5 mV/s, and the surface area was normalized based on the geometric surface area; (e) corresponding Tafel plots; and (f) electrochemical surface area.

moderate stability during the 60 h electrolysis period. However, a small amount of physical degradation of the catalyst from the electrode was observed, likely due to the continuous detachment of bubbles during the generation of the O₂ generation. Impressively, the LSV (Figure S17b) and Tafel slope values (Figure S17c) were similar to that of fresh OER samples, suggesting the robustness of our designed material. Furthermore, no significant variations in surface morphology were detected after subjecting all samples to a 60 h stability test, as observed through high-resolution SEM imaging (Figure S18).

Hydrogen Evolution Reaction (HER): Experimental and Spectroscopic Analysis. HER electrocatalysts that exhibit high activity, stability, abundance, and selectivity are ideal for cost-efficient hydrogen generation applications. The activity of HER electrocatalysts is assessed through both the kinetics and thermodynamics of the reaction at the catalyst surface. It is primarily reported using metrics, such as overpotential or current density at a specific potential. The electrocatalytic HER activity was carried out using a PANI-pf-GCC@MoS2 as the working electrode in a typical threeelectrode system with a 0.5 M H₂SO₄ aqueous electrolyte. The overpotential required to reach 10 mA/cm² was found to be 178 mV (vs RHE) (Figure 8a), and the corresponding Tafel slope value was 40 mV/decade (Figure 8b). The low Tafel slope for PANI-pf-GCC@MoS2 suggests fast kinetics of hydrogen production and that the Volmer-Heyrovsky mechanism is likely operable in which hydrogen desorption is a rate-limiting step, as previously reported. 16 Despite the much simpler fabrication scheme, the overpotential and Tafel slope values reported in this work are competitive with the

previously reported results, such as commercially available Pt/ C, Co-MoS₂, 1T-MoS₂, Au-decorated MoS₂ nanosheets, and others (Table S1). Furthermore, to understand the impact of MoS₂ and the existence of PANI-pf-GCC@MoS₂ active sites, polarization performance evaluation and Tafel slope value calculations (Figure 8b) were carried out in two control samples, namely, CC@MoS2 and PANI-pf-GCC. All these samples showed higher overpotential (284 mV for CC@MoS₂ and 536 mV for PANI-pf-GCC) and increased Tafel slope values (80 mV/decade for CC@MoS₂ and 325 mV/decade for PANI-pf-GCC), suggesting that porosity and small edges of MoS₂ as a result of PANI-pf-GCC@MoS₂ synthesis significantly improve the electrochemical activity for hydrogen evolution. EIS and ECSA calculations support this observation. A deeper understanding of the electrochemical kinetics of HER was obtained through ECSA, which assessed C_{dl} as this is a key factor in the performance of electrocatalytic water splitting. The electrocatalytic activity of a material is greatly affected by its ECSA. Generally, a superior catalyst exhibits higher C_{dl} and a larger ECSA, resulting in an enhanced electrocatalytic performance. Additionally from EIS, a Nyquist plot (Figure S19) was made, which suggested that the PANI-pf-GCC@ MoS_2 has a lower charge transfer resistance (R_{ct}) value (9 Ω) compared to other samples indicating that the porous structure and MoS₂ incorporation in the graphene matrix promoted electron transfer. Similarly, a higher capacitance value (19 mF/ cm²) was obtained for the PANI-pf-GCC@MoS₂ compared to CC-MoS₂ (9.5 mF/cm²) and PANI-pf-GCC (8 mF/cm²) suggesting enhanced intrinsic HER activities (Figure 8c).

The above results clearly demonstrated MoS₂ on N-doped porous graphene as an excellent nonmetal HER electrocatalyst.

However, several reports suggested that metal incorporation in the carbon matrix can further enhance HER performance. 11,64-66 Hence, we prepared a Ni-MoS2 hydride structure and compared the electrochemical performance with that of PANI-pf-GCC@MoS₂ to understand the metal dopant effect in our material. Indeed, a decrease of 19 mV in overpotential with a lower Tafel slope value of 37 mV/decade was observed for PANI-pf-GCC@Ni-MoS2 compared to PANI-pf-GCC@ MoS₂ (Figure 8d-f and Figure S20). The XPS survey spectrum confirmed the presence of Ni, Mo, S, O, C, and N elements in the PANI-pf-GCC@Ni-MoS2 sample, respectively (Figure S21). As deconvoluted in the high-resolution XPS spectra of Mo (Figure S22a), a Mo 3d_{5/2} binding energy of 229.1 eV can be assigned to Mo⁴⁺ in 2H-MoS₂, and a Mo 3d_{5/2} binding energy of 233.1 eV is for Mo⁶⁺ like in molybdenum trioxide. The presence of small amounts of Mo in the +6 oxidation states in all samples is consistent with the known propensity of MoS₂ to undergo edge oxidation. It is important to note that no oxysulfide peak was observed in the high-resolution S 2p XPS spectra (Figure S22b). From our electrochemical analysis, the effectiveness of the HER process correlates directly with the presence of active sites on the catalyst's surface (Figure 8). Within MoS₂, active sites can manifest along both the edge and basal planes. The activation of the thermodynamically favored basal planes could hold considerable promise for boosting the electrocatalytic performance of MoS2, as it would render all the surfaces reactive for the HER. Recent studies have demonstrated effective strategies for activating these basal planes, including platinum mixing into the structure or inducing sulfur vacancies in 2H-MoS₂.^{67,9} However, Ni doping in the basal plane is highly unfavorable and difficult as revealed by Wang et al.;⁶⁹ hence, our study did not consider this aspect because there is no theoretical or experimental evidence supporting the activation of MoS₂ basal planes following the inclusion of transition metals over the basal-plane surface. It is also noted that, in MoS₂, the primary active sites are the sulfur atoms located at the edges, whereas the basal plane of 2H-MoS₂ remains inert unless defects are present. This explains why in PANI-pf-GCC@MoS2, oxidation of the material can potentially obstruct the reactive sulfur sites, as evidenced by the Tafel slope values (Figure 8) being higher compared to those of PANI-pf-GCC@Ni-MoS2 catalysts. An observation worth noting was the high-resolution XPS of Mo 3d and S 2p in PANI-pf-GCC@Ni-MoS2, which indicated an S²⁻/Mo⁴⁺ ratio of 1.82, a significant change from the sample without Ni doping (S^{2-}/Mo^{4+} ratio of 1.35). The phenomenon can be rationalized by the formation of an atomic layer Ni(OH)₂ shell, which acts as proton acceptor sites that catalyze the HER activity during the electrocatalytic process, as indicated by both the S²⁻/Mo⁴⁺ ratio and overpotential observed for the catalysts.⁷⁰ Hence, examining the Ni 2p spectra of PANI-pf-GCC@Ni-MoS2 is crucial for assessing the oxidation state of the Ni dopant atoms and detecting the presence of nickel species such as oxides or sulfides. The deconvolution of the Ni 2p_{3/2} component (Figure S23a) reveals the prevalence of oxidized species like Ni(OH)₂ at the binding energy of 856.1 eV.⁷¹ However, the Ni and S XPS data also suggested the absence of 852.7 and 162.5 eV peak binding energies for nickel sulfide in the PANI-pf-GCC@Ni-MoS2 sample. Thus, the observed conversion in the oxidation state of Ni after HER will significantly impact the electrocatalytic performance of the PANI-pf-GCC@Ni-MoS $_2$ sample. From the N 1s spectrum (Figure S23b), we also observed a Mo-N

coordination peak at a binding energy of 400.0 eV, alongside N-pyridinic and N-graphitic peaks at binding energies of 397.7 and 401.4 eV, respectively. The deconvoluted C 1s peaks with binding energies of 284.4 eV for C–C sp², 284.9 eV for C–C sp³, 286.3 eV for C–N/O, 287.9 eV for C=O, and 283.9 eV for carbide (Figure S23c) confirmed the maintenance of the defected graphene structure as well during Ni incorporation.

XPS analysis conducted on the post-HER operation of the PANI-pf-GCC@Ni-MoS2 sample in C 1s, Mo 3d, O 1s, and N 1s elements (Figure S24) provides additional understanding regarding the destiny of the active sites. The post-HER samples were prepared by multiple cycles of LSV and then analyzing the XPS. Following the high-resolution Mo 3d and S 2p spectra analysis (Figure S24e,f), no significant changes in the S²⁻/Mo⁴⁺ ratio were detected post-HER compared to the pristine PANI-pf-GCC@Ni-MoS2. The ratio can be attributed to two potential scenarios: one possibility is that sulfur vacancies were refilled with extra sulfur atoms, although this is unlikely. Alternatively, metals might protect these vacancies during the electrocatalytic process. These hypotheses offer promising directions for a deeper investigation. From the XPS data, our primary observation of the Ni 2p_{3/2} component in the fresh and post-HER operated PANI-pf-GCC@Ni-MoS2 samples suggests an increased shift in the Ni 2p_{3/2} peak of post-HER sample to around 857.0 eV, this is the characteristic XPS peak of NiOOH. This is accompanied by an increase in the intensities of Ni 2p_{3/2} and Ni 2p_{1/2} satellite peaks (approximately 861.0 and 873.5 eV, respectively). This shift suggests that, when subjected to HER conditions, the doping Ni atoms undergo a spontaneous increase in their oxidation state, a finding that aligns with our electrochemical analysis. In their investigation conducted in 2016, Escalera-López and colleagues also documented a similar phenomenon within their experimental setup, reinforcing the observed trend. 11 This also explains why Tafel slopes of PANI-pf-GCC@Ni-MoS2 fell at 37 mV/decade (Figure 8), as the high chalcogen deficiency in the metal-to-chalcogen ratio can lead to lower active sites because of the formation of oxides such as MoO₃ at the sulfur defect due to the isovalent characteristic of S and O.72 However, having a NiOOH layer makes the metal-tochalcogen ratio less sulfur deficient during the HER process, which is attributable to the increased accessibility of active sites as the sulfur atom participates in the efficient electrochemical adsorption and desorption processes. 11,4 Given that Ni can effectively dope both Mo and S edge sites, it is reasonable to anticipate some contribution from Mo sites as well. The highresolution XPS spectra of Mo 3d and O 1s revealed a significant 40% increase in the oxygen-to-molybdenum ratio post-HER operation in PANI-pf-GCC@Ni-MoS2 samples, whereas the oxygen-to-sulfur ratio (from S 2p and O 1s) only increased by 15% compared to pristine PANI-pf-GCC@ Ni-MoS₂ samples. This phenomenon is probably attributable, although it is not fully quantified for this work, to the increased interaction between oxygen and molybdenum in the form of MoO₃ without Ni support, in contrast to the Ni-protected sulfur sites, which hinder the oxidation of sulfur atoms during the HER process. Since MoO₃ lacks catalytic activity for the HER, it is highly likely that certain Mo atoms situated at the edges remain unaffected and could potentially play a role in the HER process. It is essential to acknowledge that identifying the precise Ni doping position will be challenging, but it can be done through XPS analysis alone. Nevertheless, our XPS analysis supports the idea that the Ni-doped S edge sites will

become fully active for the HER only when Ni-doped atoms or clusters oxidize.

The stability of the HER electrocatalyst was verified over 60 h using chronoamperometry at a fixed overpotential vs RHE in 0.5 M H₂SO₄, and then LSV followed by Tafel slope value calculations (Figure S25). Impressively, no significant changes in the LSV and Tafel slope value were observed compared to that of the fresh HER sample suggesting excellent durability of our designed material for potential real-world applications. High-resolution SEM images of post-HER performance (Figure S26) indicated no significant alterations in the surface morphologies of PANI-pf-GCC@Ni-MoS2, suggesting that hydrogen gas production had a minimal impact on the film

Hydrogen Evolution Reaction (HER) in Commercial Alkaline Water Electrolyze Conditions. While most HER studies prioritize acidic media, real-world applications necessitate assessment in alkaline electrolytes. Considering the outstanding performance of PANI-pf-GCC@Ni-MoS2 for HER in an acidic medium, we investigated HER activities in 1 M KOH electrolyte solution. The J versus V graph (Figure S27) showed a slightly higher overpotential of 175 mV and a slightly higher Tafel slope value of 42 mV/decade at a current density of 10 mA/cm². The overpotentials of Ni-doped MoS₂ in acidic conditions are influenced by edge or boundary exposure, which is less active in alkaline environments. Therefore, it may be speculated that the primary HER sites shift from edges in acid to basal planes in alkaline solutions. Given that our MoS₂ lacks significant basal-plane activation (only the 1T phase of MoS2 exhibits an active basal plane for HER activation), it is anticipated to exhibit higher Tafel slope values and overpotentials when compared with acidic electrolytes. This observation is supported by an existing literature. ¹⁶ We further measured the HER activities in commercial alkaline conditions, which is 30 wt % KOH (~6M) electrolytes at 80 °C temperature. As shown in Figure S27, the PANI-pf-GCC@ Ni-MoS₂ exhibited impressive HER activities even in harsh conditions with a minimal change in the overpotential to attain the 10 mA/cm² current density. This observation indicates that our PANI-pf-GCC@Ni-MoS2 electrocatalyst is not limited to acidic media but extends its suitability to alkaline media as well. Moreover, these experiments under diverse conditions, including high-temperature environments, underline the versatility and durability of our catalyst, making it highly relevant for electrolyzer applications.

CONCLUSIONS

An energy-efficient and rapid fabrication of a porous N-doped graphene/carbon cloth substrate was demonstrated to yield high-performance electrocatalysts for both oxygen and hydrogen evolution reactions. The material was synthesized by rapid photothermal pyrolysis of a PANI-carbon cloth composite obtained by electropolymerization of PANI. Compared to conventional annealing methods, the proposed photothermal pyrolysis achieves fast pyrolysis in seconds, yielding mechanically stable mesoporous N-doped graphene structures with well-dispersed pores. This substrate enhances the electrocatalyst-substrate interconnection, which is crucial for the catalytic efficiency. SEM images showed the homogeneous distribution of N-doped graphene on a carbon cloth substrate. By electrochemically depositing and growing Ni species and MoS₂ on the N-doped graphene, the corresponding PANI-pf-GCC@Ni and PANI-pf-GCC@Ni-MoS2 materials were

obtained. Incorporating Ni and MoS2 in the N-doped graphene matrix enhanced the electrocatalysis activity toward the OER and HER under alkaline and acidic conditions, as confirmed by their lower Tafel slopes, lower overpotentials, and higher electrochemical surface area calculations. Based on XPS and DFT analysis, the exceptionally high electrocatalytic activity for the OER was attributed to the formation of Ni hydroxide species, whereas Ni doping protects MoS₂ from sulfur oxidation, maintaining stable performance ratios critical for optimal HER activity. Impressively, both electrocatalysts showed long-term durability for at least 60 h without compromising their electrochemical activity. Further, the HER activity of the PANI-pf-GCC@Ni-MoS2 material was measured under commercial alkaline conditions to understand the suitability of the material in industrial electrolyzers. These detailed findings can be a significant step toward practical and economical oxygen and hydrogen production that may stimulate broad interest in reducing fossil fuel consumption.

ASSOCIATED CONTENT

Supporting Information

The Supporting Information is available free of charge at https://pubs.acs.org/doi/10.1021/acsami.4c08869.

Experimental details, additional SEM images, XPS data, Raman data, and additional analysis of the electrochemical data (PDF)

AUTHOR INFORMATION

Corresponding Authors

Peng Bai – Department of Chemical Engineering, University of Massachusetts Amherst, Amherst, Massachusetts 01003, *United States;* orcid.org/0000-0002-6881-4663; Email: pengbai@umass.edu

James J. Watkins - Conte Center for Polymer Research, Department of Polymer Science and Engineering, University of Massachusetts Amherst, Amherst, Massachusetts 01003, *United States;* orcid.org/0000-0001-8302-825X; Email: watkins@polysci.umass.edu

Authors

Dipankar Saha - Conte Center for Polymer Research, Department of Polymer Science and Engineering, University of Massachusetts Amherst, Amherst, Massachusetts 01003, United States; orcid.org/0000-0002-6268-2807

Ayush Bhardwaj - Conte Center for Polymer Research, Department of Polymer Science and Engineering, University of Massachusetts Amherst, Amherst, Massachusetts 01003, United States; orcid.org/0000-0002-8782-2116

Jiacheng Wang - Department of Chemical Engineering, University of Massachusetts Amherst, Amherst, Massachusetts 01003, United States; orcid.org/0000-0002-7948-8525

Varun Pande - Conte Center for Polymer Research, Department of Polymer Science and Engineering, University of Massachusetts Amherst, Amherst, Massachusetts 01003,

Robert Hengstebeck – Materials Research Institute, The Pennsylvania State University, University Park, Pennsylvania 16802, United States

Complete contact information is available at: https://pubs.acs.org/10.1021/acsami.4c08869

Author Contributions

D.S.: conceptualization, investigation, data curation, writing original draft, writing—review and editing; A.B.: investigation, data curation; J.W.: investigation, theoretical analysis, data curation, writing—review and editing; V.P.: investigation, writing—review and editing; R.H.: investigation; P.B.: conceptualization, investigation, supervision, funding acquisition, writing-review and editing; and J.J.W.: conceptualization, supervision, funding acquisition, writing-review and editing.

Notes

The authors declare no competing financial interest.

ACKNOWLEDGMENTS

The authors are grateful to acknowledge the Penn State Materials Characterization Lab for the use of the XPS instrument and Mr. Jeffrey Shallenberger for helpful discussions on sample preparation and measurement; the facility services for electronic microscopy, and spectroscopy at the Department of Polymer Science and Engineering, and the Institute of Applied Sciences at the University of Massachusetts, Amherst, USA. The authors are also thankful to the Watkins group members, particularly Mr. Takumi Uchiyama, Connor Witt, and David Schechter for the fruitful discussion. P.B. acknowledges the financial support from the National Science Foundation (CBET 2144360). The computer calculations used resources of the National Energy Research Scientific Computing Center (NERSC) through allocation ERCAP0021594 and of the Advanced Cyberinfrastructure Coordination Ecosystem (ACCESS) through allocation CTS190069. J.J.W. acknowledges financial support from the US Army Research Laboratory (under the National Center for Manufacturing Sciences-award number HQ0034-15-2-0007, Expeditionary Maneuver Support award number W911QY1990011), as well as Office of Naval Research (under LIFT award number N000142190010).

REFERENCES

- (1) Reddington, E.; Sapienza, A.; Gurau, B.; Viswanathan, R.; Sarangapani, S.; Smotkin, E. S.; Mallouk, T. E. Combinatorial Electrochemistry: A Highly Parallel, Optical Screening Method for Discovery of Better Electrocatalysts. Science 1998, 280 (5370), 1735-1737.
- (2) Saha, D.; Kruse, P. Editors' Choice—Review—Conductive Forms of Mos2 and Their Applications in Energy Storage and Conversion. J. Electrochem. Soc. 2020, 167 (12), 126517.
- (3) Saha, D.; Dalmieda, J.; Patel, V. Surface-Modified Mxenes: Simulation to Potential Applications. ACS Applied Electronic Materials 2023, 5 (6), 2933-2955.
- (4) Saha, D.; Patel, V.; Selvaganapathy, P. R.; Kruse, P. Facile Fabrication of Conductive Mos2 Thin Films by Sonication in Hot Water and Evaluation of Their Electrocatalytic Performance in the Hydrogen Evolution Reaction. Nanoscale Advances 2021, 4 (1), 125-
- (5) Wang, Y.; Ding, Z.; Arif, N.; Jiang, W.-C.; Zeng, Y.-J. 2d Material Based Heterostructures for Solar Light Driven Photocatalytic H2 Production. *Materials Advances* **2022**, 3 (8), 3389–3417.
- (6) Zeng, M.; Li, Y. Recent Advances in Heterogeneous Electrocatalysts for the Hydrogen Evolution Reaction. Journal of Materials Chemistry A 2015, 3 (29), 14942–14962.
- (7) Saha, D.; Yu, H.-J.; Wang, J.; Prateek; Chen, X.; Tang, C.; Senger, C.; Pagaduan, J. N.; Katsumata, R.; Carter, K. R.; et al. Mesoporous Single Atom-Cluster Fe-N/C Oxygen Evolution Electrocatalysts Synthesized with Bottlebrush Block Copolymer-

- Templated Rapid Thermal Annealing. ACS Appl. Mater. Interfaces 2024, 16 (11), 13729-13744.
- (8) Ye, G.; Gong, Y.; Lin, J.; Li, B.; He, Y.; Pantelides, S. T.; Zhou, W.; Vajtai, R.; Ajayan, P. M. Defects Engineered Monolayer Mos2 for Improved Hydrogen Evolution Reaction. Nano Lett. 2016, 16 (2), 1097-1103.
- (9) Benson, J.; Li, M.; Wang, S.; Wang, P.; Papakonstantinou, P. Electrocatalytic Hydrogen Evolution Reaction on Edges of a Few Layer Molybdenum Disulfide Nanodots. ACS Appl. Mater. Interfaces 2015, 7 (25), 14113-14122.
- (10) Wang, D.; Zhang, X.; Shen, Y.; Wu, Z. Ni-Doped Mos2 Nanoparticles as Highly Active Hydrogen Evolution Electrocatalysts. RSC Adv. 2016, 6 (20), 16656-16661.
- (11) Escalera-López, D.; Niu, Y.; Yin, J.; Cooke, K.; Rees, N. V.; Palmer, R. E. Enhancement of the Hydrogen Evolution Reaction from Ni-Mos2 Hybrid Nanoclusters. ACS Catal. 2016, 6 (9), 6008-6017.
- (12) Stern, L.-A.; Hu, X. Enhanced Oxygen Evolution Activity by Niox and Ni(Oh)2 Nanoparticles. Faraday Discuss. 2014, 176 (0),
- (13) Yin, Y.; Han, J.; Zhang, Y.; Zhang, X.; Xu, P.; Yuan, Q.; Samad, L.; Wang, X.; Wang, Y.; Zhang, Z.; et al. Contributions of Phase, Sulfur Vacancies, and Edges to the Hydrogen Evolution Reaction Catalytic Activity of Porous Molybdenum Disulfide Nanosheets. J. Am. Chem. Soc. 2016, 138 (25), 7965-7972.
- (14) Xu, L.; Jiang, Q.; Xiao, Z.; Li, X.; Huo, J.; Wang, S.; Dai, L. Plasma-Engraved Co3o4 Nanosheets with Oxygen Vacancies and High Surface Area for the Oxygen Evolution Reaction. Angew. Chem., Int. Ed. 2016, 55 (17), 5277-5281.
- (15) Saha, D.; Angizi, S.; Darestani-Farahani, M.; Dalmieda, J.; Selvaganapathy, P. R.; Kruse, P. Tuning the Chemical and Mechanical Properties of Conductive Mos2 Thin Films by Surface Modification with Aryl Diazonium Salts. Langmuir 2022, 38 (12), 3666-3675.
- (16) Lingappan, N.; Jeon, I.; Lee, W. Polyaniline Induced Multi-Functionalities in Interfacially Coupled Electrocatalysts for Hydrogen/Oxygen Evolution Reactions. Journal of Materials Chemistry A **2023**, 11 (33), 17797–17809.
- (17) Muthurasu, A.; Maruthapandian, V.; Kim, H. Y. Metal-Organic Framework Derived Co3o4/Mos2 Heterostructure for Efficient Bifunctional Electrocatalysts for Oxygen Evolution Reaction and Hydrogen Evolution Reaction. Applied Catalysis B: Environmental 2019, 248, 202-210.
- (18) Voiry, D.; Fullon, R.; Yang, J.; de Carvalho Castro e Silva, C.; Kappera, R.; Bozkurt, I.; Kaplan, D.; Lagos, M. J.; Batson, P. E.; Gupta, G.; et al. The Role of Electronic Coupling between Substrate and 2d Mos2 Nanosheets in Electrocatalytic Production of Hydrogen. Nat. Mater. 2016, 15 (9), 1003-1009.
- (19) Wang, X.-D.; Chen, H.-Y.; Xu, Y.-F.; Liao, J.-F.; Chen, B.-X.; Rao, H.-S.; Kuang, D.-B.; Su, C.-Y. Self-Supported Nimop2 Nanowires on Carbon Cloth as an Efficient and Durable Electrocatalyst for Overall Water Splitting. Journal of Materials Chemistry A 2017, 5 (15), 7191-7199.
- (20) Feng, L.-L.; Fan, M.; Wu, Y.; Liu, Y.; Li, G.-D.; Chen, H.; Chen, W.; Wang, D.; Zou, X. Metallic Co9s8 Nanosheets Grown on Carbon Cloth as Efficient Binder-Free Electrocatalysts for the Hydrogen Evolution Reaction in Neutral Media. Journal of Materials Chemistry A 2016, 4 (18), 6860-6867.
- (21) Okoroanyanwu, U.; Bhardwaj, A.; Watkins, J. J. Large Area Millisecond Preparation of High-Quality, Few-Layer Graphene Films on Arbitrary Substrates Via Xenon Flash Lamp Photothermal Pyrolysis and Their Application for High-Performance Micro-Supercapacitors. ACS Appl. Mater. Interfaces 2023, 15 (10), 13495-13507.
- (22) Cheng, Q.; Tang, J.; Ma, J.; Zhang, H.; Shinya, N.; Qin, L.-C. Polyaniline-Coated Electro-Etched Carbon Fiber Cloth Electrodes for Supercapacitors. J. Phys. Chem. C 2011, 115 (47), 23584-23590.
- (23) Kresse, G.; Furthmüller, J. Efficiency of Ab-Initio Total Energy Calculations for Metals and Semiconductors Using a Plane-Wave Basis Set. Comput. Mater. Sci. 1996, 6 (1), 15-50.

- (24) Kresse, G.; Furthmüller, J. Efficient Iterative Schemes for Ab Initio Total-Energy Calculations Using a Plane-Wave Basis Set. Phys. Rev. B 1996, 54 (16), 11169-11186.
- (25) Yan, C.; Zou, L.; Short, R. Single-Walled Carbon Nanotubes and Polyaniline Composites for Capacitive Deionization. Desalination 2012, 290, 125-129.
- (26) Chaudhari, H. K.; Kelkar, D. S. Investigation of Structure and Electrical Conductivity in Doped Polyaniline. Polym. Int. 1997, 42 (4), 380-384.
- (27) Bhardwaj, A.; Okoroanyanwu, U.; Pagaduan, J. N.; Fan, W.; Watkins, J. J. Large-Area Fabrication of Porous Graphene Networks on Carbon Fabric Via Millisecond Photothermal Processing of Polyaniline for Supercapacitors. Small 2024, No. 2402049.
- (28) Golczak, S.; Kanciurzewska, A.; Fahlman, M.; Langer, K.; Langer, J. J. Comparative Xps Surface Study of Polyaniline Thin Films. Solid State Ionics 2008, 179 (39), 2234-2239.
- (29) Waware, U. S.; Arukula, R.; Hamouda, A. M. S.; Kasak, P. Electrochemical and X-Ray Photoelectron Spectroscopic Investigations of Conductive Polymers. Ionics 2020, 26 (2), 831-838.
- (30) Silva, R.; Voiry, D.; Chhowalla, M.; Asefa, T. Efficient Metal-Free Electrocatalysts for Oxygen Reduction: Polyaniline-Derived Nand O-Doped Mesoporous Carbons. J. Am. Chem. Soc. 2013, 135 (21), 7823-7826.
- (31) Angizi, S.; Yu, E. Y. C.; Dalmieda, J.; Saha, D.; Selvaganapathy, P. R.; Kruse, P. Defect Engineering of Graphene to Modulate Ph Response of Graphene Devices. Langmuir 2021, 37 (41), 12163-12178.
- (32) Estrade-Szwarckopf, H. Xps Photoemission in Carbonaceous Materials: A "Defect" Peak Beside the Graphitic Asymmetric Peak. Carbon 2004, 42 (8), 1713-1721.
- (33) Tseluikin, V.; Dzhumieva, A.; Tikhonov, D.; Yakovlev, A.; Strilets, A.; Tribis, A.; Lopukhova, M. Pulsed Electrodeposition and Properties of Nickel-Based Composite Coatings Modified with Graphene Oxide. Coatings 2022, 12 (5), 656.
- (34) Wang, S.; Dong, Z.; Zhang, L.; Tsiakaras, P.; Shen, P. K.; Luo, L. Atomic Scale Mechanisms of Multimode Oxide Growth on Nickel-Chromium Alloy: Direct in Situ Observation of the Initial Oxide Nucleation and Growth. ACS Appl. Mater. Interfaces 2021, 13 (1), 1903-1913.
- (35) Xiong, D.; Li, W.; Liu, L. Vertically Aligned Porous Nickel(Ii) Hydroxide Nanosheets Supported on Carbon Paper with Long-Term Oxygen Evolution Performance. Chem. - Asian J. 2017, 12 (5), 543-551.
- (36) Bagus, P. S.; Nelin, C. J.; Brundle, C. R.; Crist, B. V.; Ilton, E. S.; Lahiri, N.; Rosso, K. M. Main and Satellite Features in the Ni 2p Xps of Nio. Inorg. Chem. 2022, 61 (45), 18077-18094.
- (37) Grosvenor, A. P.; Biesinger, M. C.; Smart, R. S. C.; McIntyre, N. S. New Interpretations of Xps Spectra of Nickel Metal and Oxides. Surf. Sci. 2006, 600 (9), 1771–1779.
- (38) Mi, L.; Wei, W.; Huang, S.; Cui, S.; Zhang, W.; Hou, H.; Chen, W. A Nest-Like Ni@Ni1.4co1.6s2 Electrode for Flexible High-Performance Rolling Supercapacitor Device Design. Journal of Materials Chemistry A 2015, 3 (42), 20973-20982.
- (39) Bao, F.; Kemppainen, E.; Dorbandt, I.; Xi, F.; Bors, R.; Maticiuc, N.; Wenisch, R.; Bagacki, R.; Schary, C.; Michalczik, U.; et al. Host, Suppressor, and Promoter-the Roles of Ni and Fe on Oxygen Evolution Reaction Activity and Stability of Nife Alloy Thin Films in Alkaline Media. ACS Catal. 2021, 11 (16), 10537-10552. Louie, M. W.; Bell, A. T. An Investigation of Thin-Film Ni-Fe Oxide Catalysts for the Electrochemical Evolution of Oxygen. J. Am. Chem. Soc. 2013, 135 (33), 12329-12337.
- (40) Wang, X.; Sun, C.; He, F.; Liu, E.; He, C.; Shi, C.; Li, J.; Sha, J.; Ji, S.; Ma, L.; Zhao, N. Enhanced Hydrogen Evolution Reaction Performance of Nico2p by Filling Oxygen Vacancies by Phosphorus in Thin-Coating Ceo2. ACS Appl. Mater. Interfaces 2019, 11 (35), 32460-32468.
- (41) Liu, S.; Zhang, H.; Hu, E.; Zhu, T.; Zhou, C.; Huang, Y.; Ling, M.; Gao, X.; Lin, Z. Boosting Oxygen Evolution Activity of Nife-Ldh

- Using Oxygen Vacancies and Morphological Engineering. Journal of Materials Chemistry A 2021, 9 (41), 23697-23702.
- (42) McKay, J. M.; Henrich, V. E. Surface Electronic Structure of Nio: Defect States, ${\mathbb{Q}} {2}$ and ${\mathbb{H}}$ _{2}\$O Interactions. Phys. Rev. B 1985, 32 (10), 6764–6772.
- (43) Reina, A.; Jia, X.; Ho, J.; Nezich, D.; Son, H.; Bulovic, V.; Dresselhaus, M. S.; Kong, J. Large Area, Few-Layer Graphene Films on Arbitrary Substrates by Chemical Vapor Deposition. Nano Lett. 2009, 9 (1), 30-35.
- (44) Jansi Rani, B.; Dhivya, N.; Ravi, G.; Zance, S. S.; Yuvakkumar, R.; Hong, S. I. Electrochemical Performance of B-Nis@Ni(Oh)2 Nanocomposite for Water Splitting Applications. ACS Omega 2019, 4 (6), 10302-10310.
- (45) Zhan, B.; Liu, C.; Chen, H.; Shi, H.; Wang, L.; Chen, P.; Huang, W.; Dong, X. Free-Standing Electrochemical Electrode Based on Ni(Oh)2/3d Graphene Foam for Nonenzymatic Glucose Detection. Nanoscale 2014, 6 (13), 7424-7429.
- (46) Saha, D.; Selvaganapathy, P. R.; Kruse, P. Peroxide-Induced Tuning of the Conductivity of Nanometer-Thick Mos2 Films for Solid-State Sensors. ACS Applied Nano Materials 2020, 3 (11), 10864-10877.
- (47) Koklioti, M. A.; Bittencourt, C.; Noirfalise, X.; Saucedo-Orozco, I.; Quintana, M.; Tagmatarchis, N. Nitrogen-Doped Silver-Nanoparticle-Decorated Transition-Metal Dichalcogenides as Surface-Enhanced Raman Scattering Substrates for Sensing Polycyclic Aromatic Hydrocarbons. ACS Applied Nano Materials 2018, 1 (7), 3625-3635.
- (48) Li, H.; Zhang, Q.; Yap, C. C. R.; Tay, B. K.; Edwin, T. H. T.; Olivier, A.; Baillargeat, D. From Bulk to Monolayer Mos2: Evolution of Raman Scattering. Adv. Funct. Mater. 2012, 22 (7), 1385-1390.
- (49) Wu, W.; Ruan, Z.; Li, J.; Li, Y.; Jiang, Y.; Xu, X.; Li, D.; Yuan, Y.; Lin, K. In Situ Preparation and Analysis of Bimetal Co-Doped Mesoporous Graphitic Carbon Nitride with Enhanced Photocatalytic Activity. Nano-Micro Letters 2019, 11 (1), 10.
- (50) Lingappan, N.; Kang, D. J. Molybdenum Disulfide Nanosheets Interconnected Nitrogen-Doped Reduced Graphene Oxide Hydrogel: A High-Performance Heterostructure for Lithium-Ion Batteries. Electrochim. Acta 2016, 193, 128-136.
- (51) Hales, N.; Schmidt, T. J.; Fabbri, E. Reversible and Irreversible Transformations of Ni-Based Electrocatalysts During the Oxygen Evolution Reaction. Current Opinion in Electrochemistry 2023, 38,
- (52) Swesi, A. T.; Masud, J.; Nath, M. Nickel Selenide as a High-Efficiency Catalyst for Oxygen Evolution Reaction. Energy Environ. Sci. 2016, 9 (5), 1771-1782.
- (53) Salarizadeh, P.; Askari, M. B.; Seifi, M.; Rozati, S. M. Mos2 Coating on Different Carbonaceous Materials: Comparison of Electrochemical Properties and Hydrogen Evolution Reaction Performance. J. Electroanal. Chem. 2019, 847, No. 113198.
- (54) Li, W.; Zhang, Z.; Zhang, W.; Zou, S. Mos2 Nanosheets Supported on Hollow Carbon Spheres as Efficient Catalysts for Electrochemical Hydrogen Evolution Reaction. ACS Omega 2017, 2 (8), 5087 - 5094.
- (55) Yeh, C.-H.; Ho, J.-J. Oxidation of Co on a Carbon-Based Material Composed of Nickel Hydroxide and Hydroxyl Graphene Oxide, (Ni4(Oh)3-Hgo) - a First-Principles Calculation. Phys. Chem. Chem. Phys. 2015, 17 (11), 7555-7563.
- (56) Zhang, L.; Jia, Y.; Gao, G.; Yan, X.; Chen, N.; Chen, J.; Soo, M. T.; Wood, B.; Yang, D.; Du, A.; Yao, X. Graphene Defects Trap Atomic Ni Species for Hydrogen and Oxygen Evolution Reactions. Chem. 2018, 4 (2), 285-297.
- (57) Feng, C.; Faheem, M. B.; Fu, J.; Xiao, Y.; Li, C.; Li, Y. Fe-Based Electrocatalysts for Oxygen Evolution Reaction: Progress and Perspectives. ACS Catal. 2020, 10 (7), 4019-4047.
- (58) Hansen, H. A.; Rossmeisl, J.; Nørskov, J. K. Surface Pourbaix Diagrams and Oxygen Reduction Activity of Pt, Ag and Ni(111) Surfaces Studied by Dft. Phys. Chem. Chem. Phys. 2008, 10 (25), 3722 - 3730.

- (59) Wang, X.; Yang, Y.; Diao, L.; Tang, Y.; He, F.; Liu, E.; He, C.; Shi, C.; Li, J.; Sha, J.; et al. Ceox-Decorated Nife-Layered Double Hydroxide for Efficient Alkaline Hydrogen Evolution by Oxygen Vacancy Engineering. ACS Appl. Mater. Interfaces 2018, 10 (41), 35145–35153.
- (60) Song, F.; Busch, M. M.; Lassalle-Kaiser, B.; Hsu, C.-S.; Petkucheva, E.; Bensimon, M.; Chen, H. M.; Corminboeuf, C.; Hu, X. An Unconventional Iron Nickel Catalyst for the Oxygen Evolution Reaction. ACS Central Science 2019, 5 (3), 558–568.
- (61) Radinger, H.; Connor, P.; Tengeler, S.; Stark, R. W.; Jaegermann, W.; Kaiser, B. Importance of Nickel Oxide Lattice Defects for Efficient Oxygen Evolution Reaction. *Chem. Mater.* **2021**, 33 (21), 8259–8266.
- (62) Zhou, W.; Cao, X.; Zeng, Z.; Shi, W.; Zhu, Y.; Yan, Q.; Liu, H.; Wang, J.; Zhang, H. One-Step Synthesis of Ni3s2 Nanorod@ Ni(Oh)2nanosheet Core—Shell Nanostructures on a Three-Dimensional Graphene Network for High-Performance Supercapacitors. *Energy Environ. Sci.* 2013, 6 (7), 2216–2221.
- (63) Miao, J.; Xiao, F.-X.; Yang, H. B.; Khoo, S. Y.; Chen, J.; Fan, Z.; Hsu, Y.-Y.; Chen, H. M.; Zhang, H.; Liu, B. Hierarchical Ni-Mo-S Nanosheets on Carbon Fiber Cloth: A Flexible Electrode for Efficient Hydrogen Generation in Neutral Electrolyte. *Science Advances* **2015**, *1* (7), No. e1500259.
- (64) Shi, Y.; Zhou, Y.; Yang, D.-R.; Xu, W.-X.; Wang, C.; Wang, F.-B.; Xu, J.-J.; Xia, X.-H.; Chen, H.-Y. Energy Level Engineering of Mos2 by Transition-Metal Doping for Accelerating Hydrogen Evolution Reaction. *J. Am. Chem. Soc.* **2017**, *139* (43), 15479–15485.
- (65) Liu, X.; Gong, L.; Wang, L.; Chang, C.; Su, P.; Dou, Y.; Dou, S. X.; Li, Y.; Gong, F.; Liu, J. Enabling Ultrafine Ru Nanoparticles with Tunable Electronic Structures Via a Double-Shell Hollow Interlayer Confinement Strategy toward Enhanced Hydrogen Evolution Reaction Performance. *Nano Lett.* **2024**, 24 (2), 592–600.
- (66) Gong, F.; Liu, Y.; Zhao, Y.; Liu, W.; Zeng, G.; Wang, G.; Zhang, Y.; Gong, L.; Liu, J. Universal Sub-Nanoreactor Strategy for Synthesis of Yolk-Shell Mos2 Supported Single Atom Electrocatalysts toward Robust Hydrogen Evolution Reaction. *Angew. Chem., Int. Ed.* **2023**, *62* (40), No. e202308091.
- (67) Deng, J.; Li, H.; Xiao, J.; Tu, Y.; Deng, D.; Yang, H.; Tian, H.; Li, J.; Ren, P.; Bao, X. Triggering the Electrocatalytic Hydrogen Evolution Activity of the Inert Two-Dimensional Mos2 Surface Via Single-Atom Metal Doping. *Energy Environ. Sci.* **2015**, 8 (5), 1594–1601.
- (68) Lawrence, N. S.; Davis, J.; Compton, R. G. Analytical Strategies for the Detection of Sulfide: A Review. *Talanta* **2000**, *52* (5), 771–784.
- (69) Wang, H.; Tsai, C.; Kong, D.; Chan, K.; Abild-Pedersen, F.; Nørskov, J. K.; Cui, Y. Transition-Metal Doped Edge Sites in Vertically Aligned Mos2 Catalysts for Enhanced Hydrogen Evolution. *Nano Res.* **2015**, *8* (2), 566–575.
- (70) Escalera-López, D.; Gómez, E.; Vallés, E. Electrochemical Growth of Coni and Pt-Coni Soft Magnetic Composites on an Alkanethiol Monolayer-Modified Ito Substrate. *Phys. Chem. Chem. Phys.* **2015**, *17* (25), 16575–16586.
- (71) Biesinger, M. C.; Payne, B. P.; Lau, L. W. M.; Gerson, A.; Smart, R. S. C. X-Ray Photoelectron Spectroscopic Chemical State Quantification of Mixed Nickel Metal, Oxide and Hydroxide Systems. *Surf. Interface Anal.* **2009**, 41 (4), 324–332.
- (72) Chen, Z.; Cummins, D.; Reinecke, B. N.; Clark, E.; Sunkara, M. K.; Jaramillo, T. F. Core–Shell Moo3–Mos2 Nanowires for Hydrogen Evolution: A Functional Design for Electrocatalytic Materials. *Nano Lett.* **2011**, *11* (10), 4168–4175.